The Dissertation Committee for Zhongping Chen certifies that this is the approved version of the following dissertation:

Magnetic Equilibrium and Transport Modeling of Divertors for Solutions to Exhaust Problems in Tokamaks

Committee:

Swadesh M Mahajan, Supervisor

Richard D Hazeltine, Co-Supervisor

Michael T Kotschenreuther

Philip J Morrison

Lorenzo A Sadun

Magnetic Equilibrium and Transport Modeling of Divertors for Solutions to Exhaust Problems in Tokamaks

by

Zhongping Chen, B.E.

Dissertation

Presented to the Faculty of the Graduate School of
The University of Texas at Austin
in Partial Fulfillment
of the Requirements
for the degree of
Doctor of Philosophy

The University of Texas at Austin
May, 2017

Magnetic Equilibrium and Transport Modeling of Divertors for Solutions to Exhaust Problems in Tokamaks

by

Zhongping Chen, Ph.D.

The University of Texas at Austin, 2017

Supervisors: Swadesh Mahajan and Richard Hazeltine

Problems of intense exhaust heat and particle fluxes incident on material surfaces are obstacles for magnetic confinement fusion in tokamaks. Advanced divertors offer magnetic solutions to the problems by (a) increasing the plasma-wetted area via flux expansion at the targets, (b) increasing the connection length and (c) in the case of X-divertors opening regimes of stable, detached operation via poloidal flaring. By magnetic equilibrium modeling using CORSICA code, X-divertors appear feasible on NSTX-U tokamak, requiring no hardware change and respecting coil current limits. Transport simulations using SOLPS code on NSTX-U have demonstrated the advantages of the X-divertor over the standard divertor: reducing target heat and particle fluxes, achieving detachment with a lower upstream density and stabilizing the detachment front near the target.

Contents

Chapter 1

Divertor Applications in Tokamak

In this chapter a brief history of tokamak divertors is given. Starting with limiters, I will address the evolving exhaust problems in tokamak research as we advance towards thermonuclear fusion. Then I will introduce the revolutionary concept of a divertor and explain various classes of divertor magnetic geometries. New challenges in the power exhaust problem, that have led to the advanced divertor research, are also addressed at the end of the chapter.

1.1 "Limited" Plasma

Plasma in a tokamak is confined by a helical magnetic field (Fig. A.2). However, since the confinement is not perfect, there is transport of particles and heat perpendicular to the field lines (or flux surfaces) commonly known as cross-field transport. (The difference between actual cross-field transport and the neoclassical expectation is called *anomalous transport*, which often exceeds eeoclassical expectations by an order of magnitude or more. It is generally assumed that anomalous transport is generated by turbulence due to micro-instabilities.) Anomalous transport is inevitable in reality in a fusion reactor. As a result, exhaust plasma will be in contact with the wall of the vacuum vessel. The plasma is essentially limited by the solid vessel just like in the case of a discharge tube (fluorescent lights and neon signs).

The first and fourth state of matter (solid and plasma) do not co-exist easily. Erosion, due to the impact of plasma particles, can become a serious problem as the plasma temperature rises. The eroded particles can contaminate the plasma, making it difficult to reach fusion conditions; erosion also leads to unacceptably short lifetimes of *Plasma Facing Components* (PFCs); in fact, at high enough temperature the exhaust plasma can even melt the solid wall. One challenge for magnetic confinement fusion is to find a solution that will allow these two mutually irritating states

of matter to cohabit a relatively limited space.

One early solution was to use a *limiter* inside the vacuum vessel to limit the expansion of the plasma. Charged particles diffuse very slowly across magnetic fields, compared with their unrestricted motion along the field lines. In a tokamak this means that the radial diffusion of the charged particles is much slower than the particle motion in the toroidal direction. The limiter solution, the insertion of a solid barrier inside the vessel (Fig. 1.1), makes use of this fact.

The charged particles that diffuse outside a certain radius a will hit the limiter and be removed from the plasma before they reach the wall. (The removal mechanism is recycling. Ions and electrons reach the wall at the same flow rate. Thus effectively an ion picks up an electron before it reaches the wall and a neutral particle is released in return.) This way the plasma is limited within the radius a (the *minor radius*) and separated from the solid wall. The boundary of the plasma is determined by the last flux surface, going outwards from the main plasma, that does not touch the limiter. It is called the *last closed flux surface*, or LCFS for short. Surfaces radially further in are all *closed* while those further out are all *open*, open in the sense that they intersect some solid surface. The plasma inside the LCFS is the main plasma, commonly referred to as the *core*, while the plasma outside the LCFS is in direct contact with solid surface and generally referred to as the *scrape-off layer* or *SOL*.

The wall is protected by the limiter from contact with the plasma. However such protection does not come for free. Instead of spreading over a large area of the vessel wall, the plasma–surface interaction is concentrated on a thin area on the limiter. The interaction area is called the *plasma-wetted area*. Shrinking the wetted area tends to cause localized over-heating and other problems. Regardless of these problems, it was hoped in the early days that the SOL "would take care of itself " and using limiters would just be fine. The edge region was not of primary interest to the main thrust of the fusion research at that time.

As fusion research progressed, it became apparent that the SOL was not in fact going to "take care of itself", and that the plasma edge could not be ignored but rather required significant attention. The plasma temperature of the core was determined by the balance of plasma heating and the loss due to impurity radiation. As fusion performance improved and plasma temperatures rose, the heat fluxes over the wetted area increased dramatically, which resulted in intense sputtering. Because of

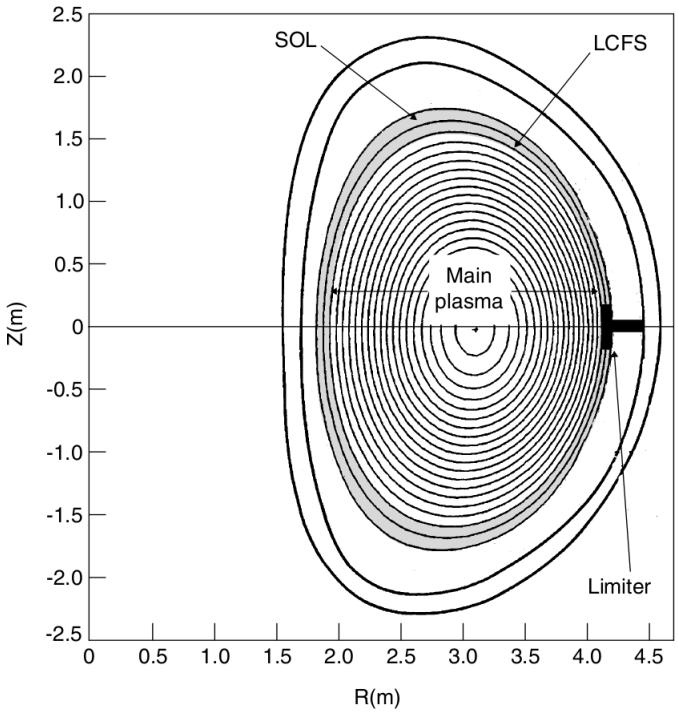

Figure 1.1: The limiter concept for a tokamak. The LCFS is determined by the leading edge of the limiter. Outside the LCFS is the SOL. Picture courtesy of P. Stangeby [28].

the proximity of the limiter and the core, the higher-Z ions sputtered off the solid surface found their way into the plasma core easily. The radiation from these high-Z impurities caused a significant amount of energy loss in the core. The radiative cooling was so strong that core could not be heated to higher temperatures. The tokamaks with limiters had reached a bottleneck.

1.2 Diverted Plasma

Although sputtering due to the contact of the plasma and the solid wall is inevitable, it is possible to move the contact area far away from the core plasma such that the sputtered high-Z ions do not find it easy to contaminate the core. This was the genesis of the concept of a *diverted* plasma. The *divertor* idea uses the concept of a magnetic *X-point* that is created by two parallel currents going in the same direction. As shown in Fig. 1.2, at some point between the two parallel currents, a null point exists where the in-plane component of the magnetic field is zero. The magnetic

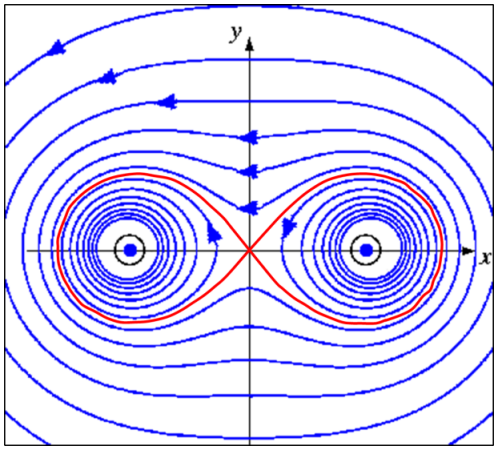

Figure 1.2: An X-point appears in the magnetic field of two parallel currents. Picture courtesy of D. Kacprzak [1].

field line (flux surface) makes a "figure 8" shape giving the null point the name —the magnetic X-point. It should be noted that the total magnetic field is not necessary zero at the X-point.

One can create an X-point inside a tokamak by introducing a toroidal current, I_D, that goes in the same direction as the plasma current, I_P as shown in Fig. 1.3. By a careful design, one can place the "figure-8" such that the lobe with the I_D in the center is truncated by the wall of the vessel. In this way, the core is confined in the lobe containing I_P and the exhaust plasma transported outside the boundary of the "figure-8" is diverted and in contact with the solid wall at a place far away from the core.

When a divertor is employed in a tokamak, three distinct types of regions are created around the x-point(s): the core, the SOL and the *private region*. Inside the core, the flux surfaces are closed while in the SOL and the private region, the flux surfaces are open. These three regions are separated by the LCFS, which, in the context of a diverted plasma, is also called the *separatrix*. One can also divert the SOL in more than one direction, for example by introducing two X-points. The structures with one or two X-points close to the core are known as the *single-null* and *double-null* topologies. Fig. 1.4 shows the two topologies.

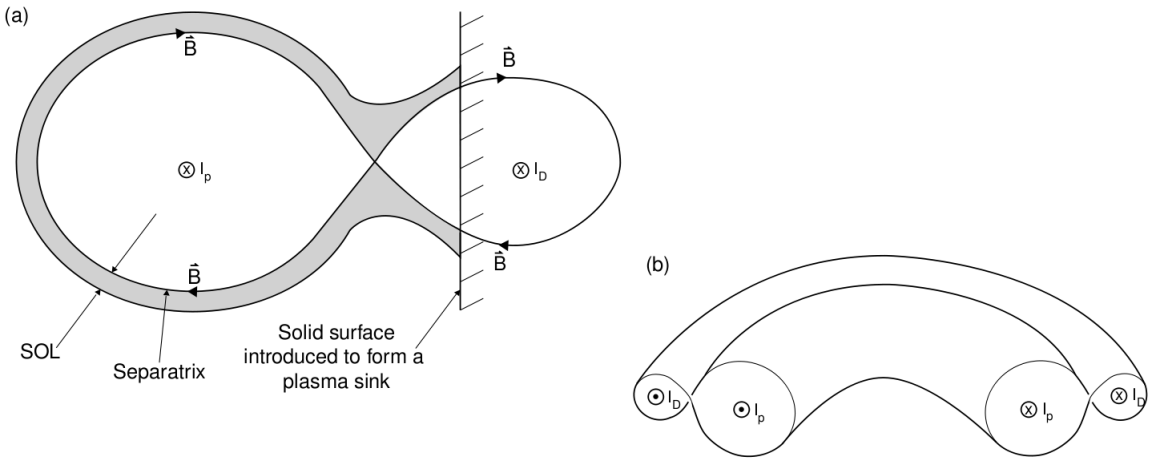

Figure 1.3: Diverted plasma. Picture courtesy of P. Stangeby [28].

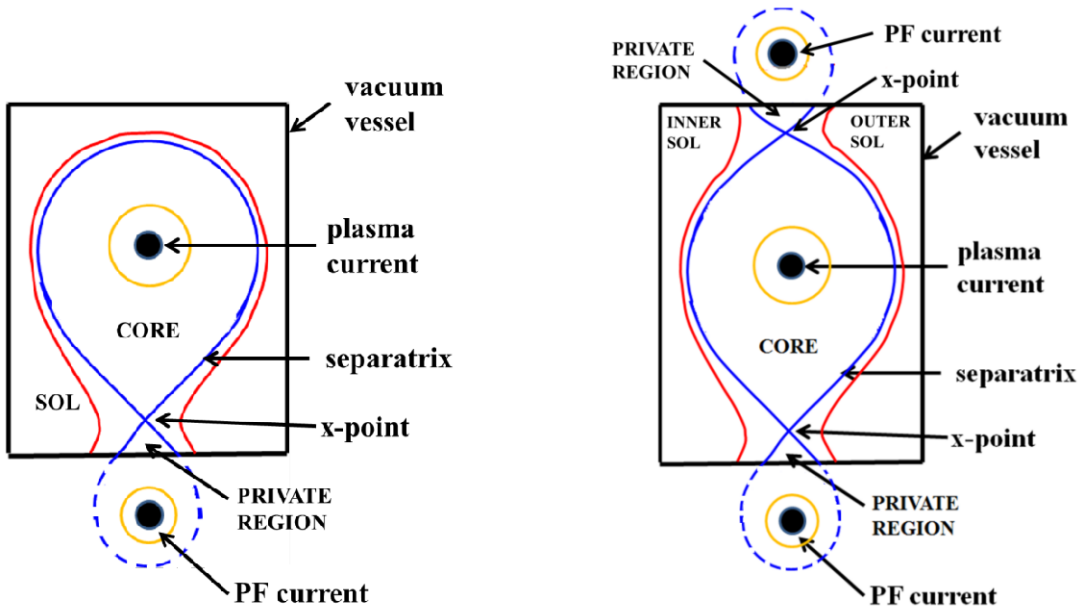

Figure 1.4: Single and double null topologies of diverted plasmas.

The concept of a divertor proved to be revolutionary; it allowed fusion research to enter a region of higher core temperature. However, as the triple product (see Appendix A.2) increases on the way to fusion, a conventional divertor's ability to handle the increasing exhaust power and particle fluxes is already challenged. In 1982 the so-called "High-Confinement Mode," or H-mode, was discovered on the ASDEX tokamak. In an H-mode plasma, a transport barrier, the *pedestal*, appears right inside the separatrix. By suppressing anomalous transport, the pedestal greatly improved the core energy confinement. Since then, H-mode has been considered an essential state that a fusion grade plasma has to be in. However in an H-mode, there is a minimum exhaust power needed to sustain the barrier. Hence, all the power cannot be dissipated by radiation in the core, and significant power must flow to the SOL and to the wall. For a fusion grade plasma, this produces very large heat fluxes on PFCs. As the core energy confinement is improved, the exhaust power and particle fluxes rise too. Furthermore, in an H-mode plasma, there are *edge-localized modes*, ELMs, abrupt, intermittent flows of heat into the upstream SOL. Divertor targets are hit by spikes of heat and particle flows during ELMs. These features of H-mode have been pushing the limit of exhaust mitigation capabilities a conventional divertor can deliver.

It was realized that the exhaust heat of future tokamaks will push beyond the cooling capability of the standard divertor (SD) which is employed in most of the current machines including ITER. The heat and particle exhaust problem will soon be so serious that innovative approaches must be developed now in quest for fusion power in the future.

This research studies the *X-divertor*, which is one of the advanced divertor designs available today.

Chapter 2

SOL Physics and Advanced Divertor Design

Various advanced divertors are introduced in this chapter with the emphasis on solving the power exhaust problems.

Basic SOL physics is covered with simple models in the first section. These easily understandable pieces of physics give heuristic ideas for advanced divertor designing.

Then in the second section advanced divertors are introduced one by one. They are first discussed from purely geometric points of view and then the manifestation of the SOL physics in their performance is made specific. A classification metric for the various divertors is presented at the end.

2.1 Basic Concepts of SOL Physics

A full description of SOL plasma needs a kinetic approach, solving Vlasov equations, because the collisionality is not strong enough. However, kinetic approach is very complicated by itself, not to mention the added complication due to the SOL magnetic geometry. Currently, there is no existing numerical code that handles SOL simulations using a kinetic approach in a 3-dimensional fashion. The fluid approach, on the other hand, is relatively simpler than the kinetic approach. In some cases, the required collisionality for a fluid approach is marginally satisfied in the SOL. From the foregoing considerations the fluid approach is indicated as possibly being adequate. Most SOL modelings to date have adopted the fluid approximation.

A fluid description of SOL involves solving the Braginskii equations (Appendix C). Though simpler than kinetic equations, the Braginskii equations are still complicated enough such that one has to use numerical simulations in order to understand the behavior of SOL plasma.

Thus a simple model is worth considering for the purpose of getting some quick and intuitive ideas of the SOL physics. Here a simple 1-dimensional SOL model is introduced and discussed in order to explain some underlying arguments for advanced divertor designs.

Anomalous transport is many times weaker than the transport processes along magnetic field lines. It is reasonable, therefore, to develop a minimal SOL model by ignoring the anomalous transport, and considering only the physics along the field line. One can thus simplify the SOL into a 1-dimensional flux tube. Let's consider the energy balance equation for this 1D tube.

$$\frac{\mathrm{d}E}{\mathrm{d}t} + \frac{\mathrm{d}Q_\parallel}{\mathrm{d}l} = R \tag{2.1}$$

where, E is the energy density, $Q_\parallel = \boldsymbol{Q} \cdot \boldsymbol{B}$ is the *parallel heat flux*, l is the coordinate along the field line and R is the source term. Often the dominant heat conduction is from the (rapid) electrons, and can be adequately described by classical Spitzer heat conduction in which case $Q_\parallel$ can be written as a function of plasma temperature T_e,

$$Q_\parallel = \kappa_0 T_e^{5/2} \frac{\mathrm{d}T_e}{\mathrm{d}l} \tag{2.2}$$

where κ_0 is a constant for Spitzer conductivity. Let us first consider the lowest order case where $R = 0$. For a steady state solution, $Q_\parallel$ is constant along the field line. In this case T_e can be solved as,

$$T_e^{7/2} = \frac{7 Q_\parallel l}{2\kappa_0} + \text{Constant} \tag{2.3}$$

which gives a simple relation between the plasma temperature and the distance along the field line from the target.

Let $l = 0$ be at the downstream (target) end of the 1D tube and $l = L$ be at the upstream end of the tube. Denote the downstream quantities with a subscript d and upstream quantities with a subscript u. We have

$$L Q_\parallel = \kappa_0 \left(T_{e,u}^{7/2} - T_{e,d}^{7/2} \right) \approx \kappa_0 T_{e,u}^{7/2} \tag{2.4}$$

since $T_{e,d} \ll T_{e,u}$. The upstream temperature can then be expressed as

$$T_{e,u} \sim \left(L Q_\parallel \right)^{2/7} \tag{2.5}$$

Consider the simple case in which $T_i = T_e$, $n_i = n_e$ and pressure $p = 3k_B n_e T_e$ is constant along the tube. For a given upstream density $n_{e,u} = n_e(L)$, the pressure also has the relation, using (2.5),

$$p \sim \left(LQ_\parallel\right)^{2/7} \tag{2.6}$$

At the target end of the 1D tube, the boundary condition asserts that (see section C.1 for example)

$$Q_\parallel \sim n_{e,d} T_{e,d} v_{th,e} \tag{2.7}$$

where $v_{th,e} = \sqrt{k_B T_e / m_e}$ is the electron thermal velocity. Thus,

$$Q_\parallel \sim n_{e,d} T_{e,d}^{3/2} \sim p T_{e,d}^{1/2} \sim n_{e,u} T_{e,u} T_{e,d}^{1/2} \tag{2.8}$$

Using (2.5) for $T_{e,u}$, we have an expression for downstream temperature

$$T_{e,d} \sim \frac{Q_\parallel^{10/7}}{n_{e,u}^2} \frac{1}{L^{4/7}} \tag{2.9}$$

The above conclusions based on the 1-D fluid model are valid when the characteristic length L is big compared to the mean free path l_{mfp}, which is true in a desired operating regieme for fusion reaction. For example, in the context of this research, L is on the order of meters while l_{mfp} (for either the electrons or the ions) is on the order of 10^{-2} meters in the divertor region.

Next let us consider the energy source, or rather sink, term R. This term involves three energy exchange channels — charge exchange, atomic radiation and volume recombination.

Charge exchange is a process where an ion and a neutral atom come close to each other and the electron hops from the neutral atom to the ion (Fig. 2.1). It is a process that involves very little energy or momentum change to either the ion or to the neutral. In the context of SOL physics in the divertor region, charge exchange processes generally happen between a hot ion and a cold neutral. Energy is removed from the plasma. So it is an energy loss and contributes to a sink term in R.

The next channel is atomic radiation. When an electron hits a neutral (or partially ionized impurity ion) in an inelastic collision, it excites the electron of the neutral atom (or impurity ion) to a higher energy state or ionizes it. As the electron returns to a lower energy state or the ground state, a photon is emitted. Energy is transferred

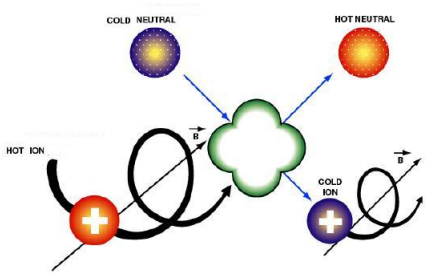

Figure 2.1: Charge exchange process.

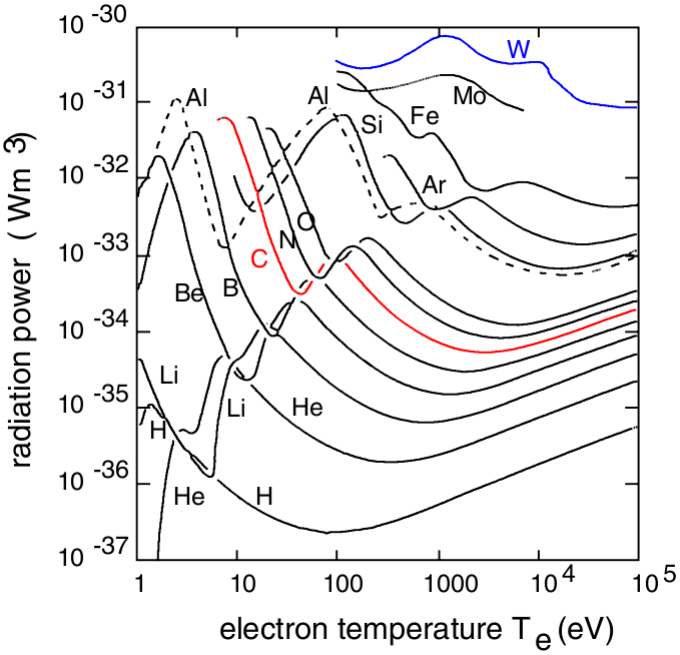

Figure 2.2: Radiation power $P_{rad}/Vol \cdot n_e \cdot n_{imp}$ as a function of electron temperature. [26, 2]

from the incident electron to the neutral (or impurity ion) and eventually carried away by the photon. If ionization occurs, the ionization energy, plus possible additional radiation, is removed from the electron. Thus atomic radiation is also an energy loss channel which contributes to a sink term in R. Shown in Fig. 2.2 is the radiation power of different atomic species. Note that impurity radiation is much stronger than

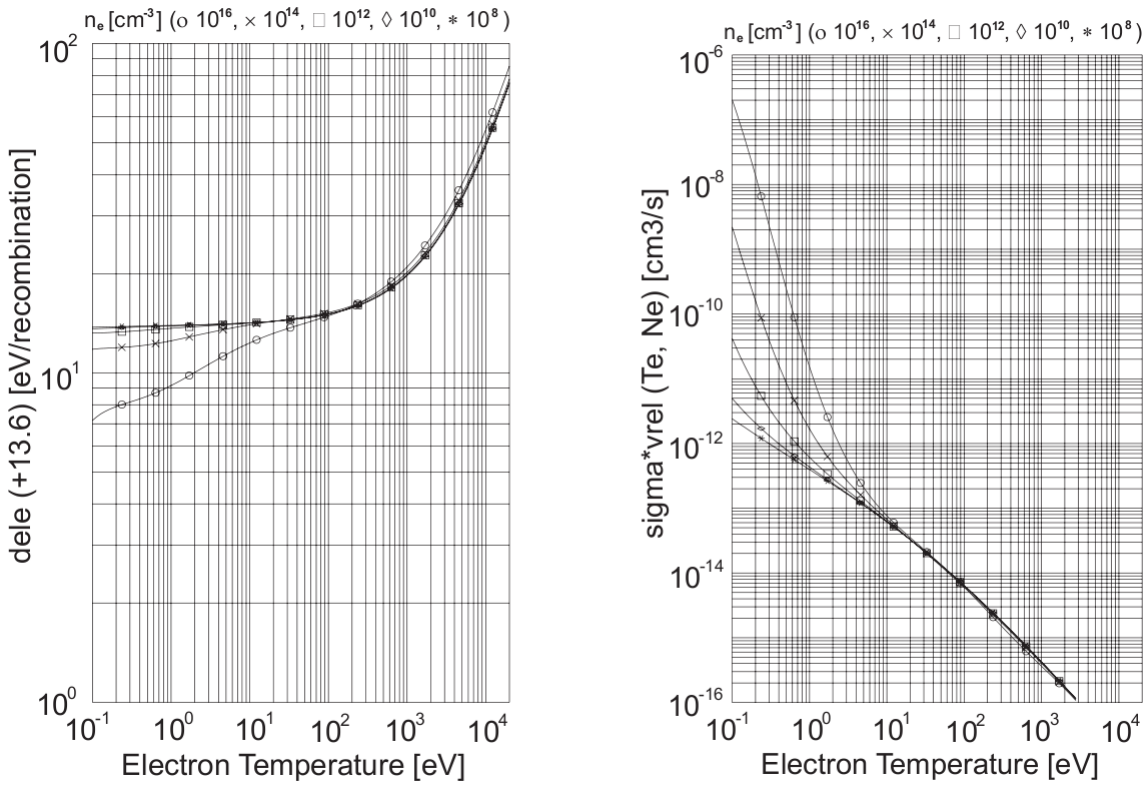

Figure 2.3: Effective electron cooling rate (in eV/recombination) due to radiation and three-body recombination as a function of electron temperature (in eV) for different electron densities (in cm^{-3}) (left). Effective hydrogenic recombination rate (in cm^3/s) as a function of electron temperature (in eV) (right). [26]

hydrogen radiation and that carbon radiation is strong when $T_e \sim 10\mathrm{eV}$. This is useful for divertor design which will be talked about in the next section.

The last channel is volume recombination. It needs a third body to account for energy and momentum conservation during the recombination process of an electron and an ion into a neutral atom. There are two possibilities: radiative recombination and three-body recombination. In the process of radiative recombination a photon takes care of energy and momentum conservation. In a three-body recombination process an additional electron ('spectator electron') is necessary. Both processes proceed in a ladder-like way through the excited levels of the atoms until the final ground state is reached. This is an energy loss channel as well. Fig. 2.3 shows typical recombination rates and cooling rates as a function of temperature for hydrogen.

Equipped with these basic concepts of SOL physics, we are in a position to discuss advanced divertors.

2.2 Advanced Divertors

2.2.1 The goal of advanced divertor designing

As mentioned in chapter 1, future tokamaks' heat and particle fluxes will soon push past the mitigation capabilities that a (soon to be described) standard divertor (SD) geometry can deliver. The heat flux of SOL depends on the exhaust power from the core to the SOL and the SOL width which is defined as the e-folding width of the radial heat flux profile at the outer midplane (see Fig. 2.4). As the core is heated to higher temperatures, and the tokamak size is scaled up, the exhaust power increases dramatically. However the SOL width does not increase proportionally. Thus the SOL heat flux will increase. According to Andrei Kukushkin the standard divertor, designed for ITER, has substantial margin for a 5 mm width, but almost none at 1mm. However the SOL width for ITER projected, for instance, by the Goldston model [3] is about 1mm. Then the standard divertor will have a problem.

Another serious problem besides the exhaust heat flux is target erosion due to sputtering, which shortens the lifetime of PFCs and contaminates the plasma.

The invention of advanced divertor was stimulated by the inadequacy of traditional means to handle heat flux and other PFC problems. The goals of advanced divertor designing include reducing the heat flux reaching the divertor target and reducing sputtering, attaining acceptable erosion.

One rule has to be followed when designing advanced divertors: the core confinement quality should not be sacrificed as the price to reduce target heat load. After all, the purpose of divertors is to allow an enhanced core confinement with higher core temperature, and to eventually reach fusion. Thus it will be meaningless to degrade the core confinement (H-mode) upstream in order to save the target downstream.

The merit of a new divertor design must be judged on what it does to the *perpendicular heat flux* ($Q_\perp = \boldsymbol{Q} \cdot \mathbf{n}$ with $\mathbf{n}$ being the unit normal vector at the target surface) at the target, and the temperature (T_e) profile from upstream to downstream. What one must seek is that $Q_\perp$ and T_e downstream are as low as possible ($T_{e,d}$ <10eV

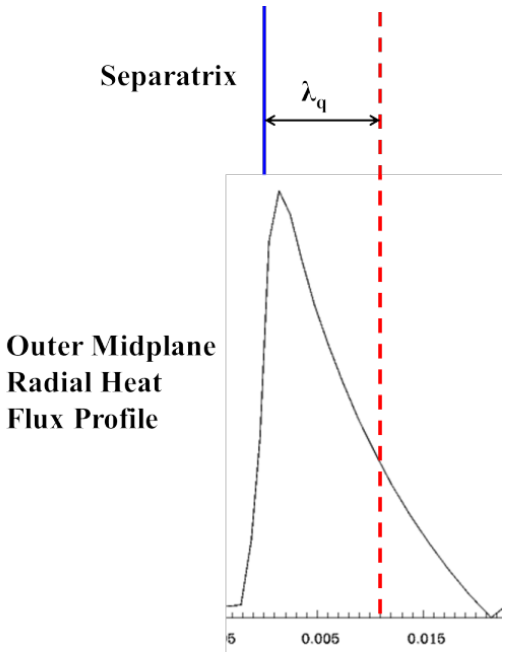

Figure 2.4: In this work, the power SOL width is measured as the e-folding width of the radial heat flux profile at the outer midplane.

, and preferably lower for acceptable erosion) simultaneous with a high upstream $T_{e,u}$.

2.2.2 Advanced divertor geometries

A simple and direct way of handling the heat flux problem is purely geometrical —tilting the target plates so that they become more oblique with respect to the incoming magnetic field lines of the SOL. This way the projected area of the SOL on the target (wetted area) is expanded and thus the heat flux is reduced. This idea is often used in standard divertor designs with the so-called *vertical target*, which is adopted in tokamaks like Alcator C-Mod (Fig. 2.5), ASDEX-U, JET and ITER.

Ideally then by making the targets almost parallel with the field line, one can expand the wetted area approaching infinity. However, this is not achievable in reality. Since the ions and electrons gyrates along the field line with Larmor radii, even if the target were perfectly parallel to the field line, the ions and electrons would still strike the target when the target came within extent of their Larmor radii. Furthermore, to avoid the so-called *hot spots*, a degree of tilting of the target tiles is required. This

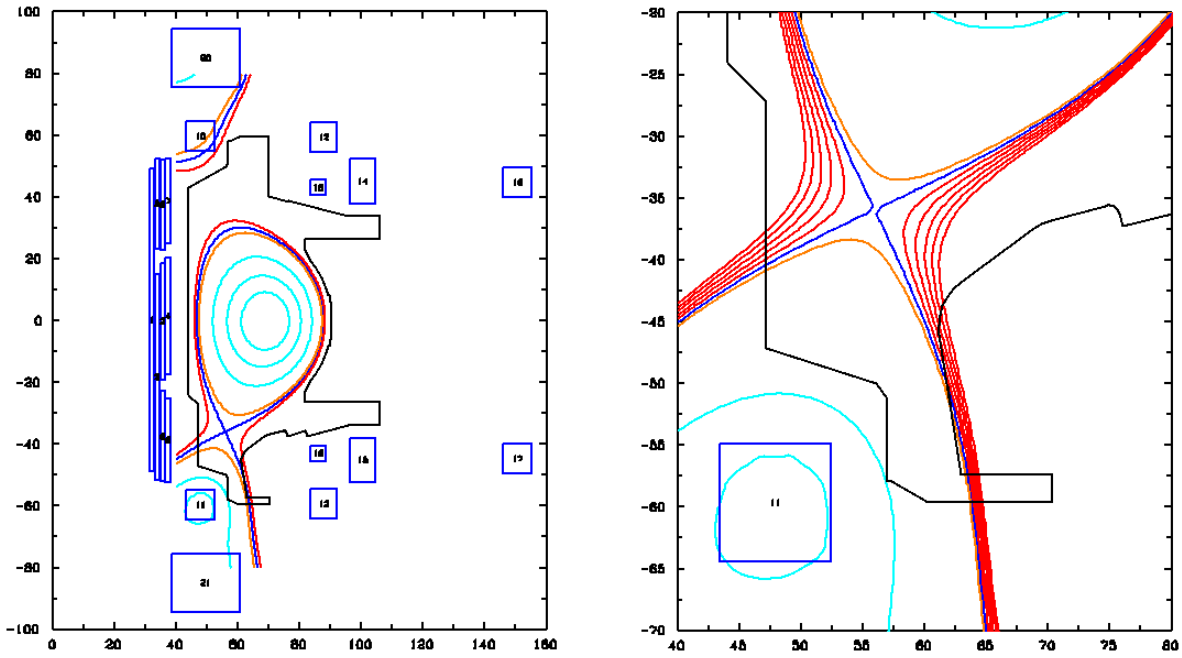

Figure 2.5: A standard divertor for C-Mod. The outboard target of C-Mod is very oblique with respect to the incident field to increase the plasma-wetted area. Figure courtesy of Brent Covele [11].

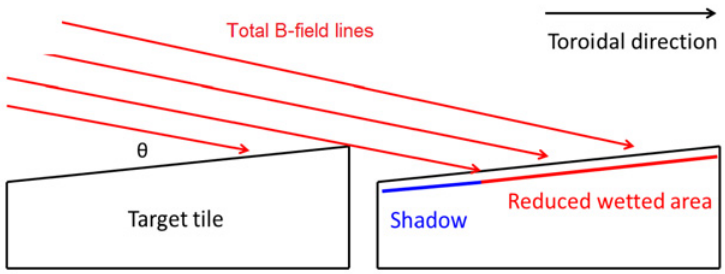

Figure 2.6: A simple illustration of shadowing on target tiles. In an attached plasma, the total wetted area is reduced as θ becomes very small. Figure courtesy of Brent Covele [10].

introduces "shadowing" (see Fig. 2.6) which places an effective limit on the useful angle of about 1°—otherwise shadowing eliminates the apparent increase in wetted area from lower angles.

Standard divertors with tilted targets are not likely to solve the heat flux problem. The advanced divertors , based on a nontrivial redesign of the magnetic geometry,

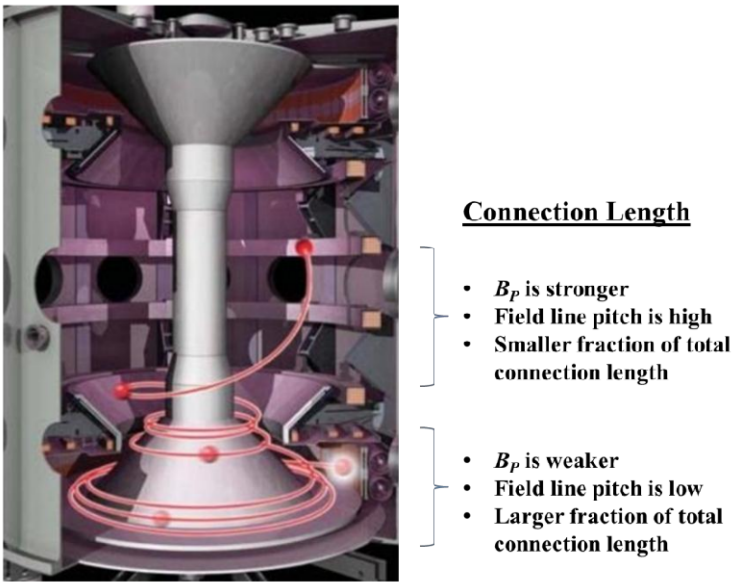

Figure 2.7: An illustration of an average particle trajectory along a field line in the MAST. The connection length is measured along the trajectory. MAST picture courtesy of the University of York [4].

attempt to solve the exhaust problem by means more encompassing than simply increasing the wetted area. The design of these configurations incorporates several features suggested by the simple SOL physics mentioned in section 2.1. As indicated by equations 2.5 and 2.9, $T_{e,u}$ and $T_{e,d}$ depends on the length of the flux tube L. Then if one wants $T_{e,u}$ to be high and $T_{e,d}$ to be low the simplest thing to do is to increase the length L, the *connection length* (Fig. 2.7). The connection length is the distance measured along the field line in 3D space from a point on the field line to the strike point where the field line intersects the target. It will be shown in the next section that an increase in L can increase impurity radiation as well.

A trivial way to increase L is to move the divertor target farther away, and hence extend the divertor leg. Nevertheless, this means to expand the dimensions of the vacuum vessel and the TF coils. The cost is too high to be practical. Also in such kind of configuration the core plasma only occupies a relatively small portion of the vacuum vessel, or rather the *magnetic volume*, making it very inefficient.

Instead of trivially changing the hardware dimensions, a smart way to increase L is to manipulate the magnetic field itself using *poloidal flux expansion*. The total

magnetic field of the SOL can be decomposed as

$$\boldsymbol{B} = \boldsymbol{B}_t + \boldsymbol{B}_p \tag{2.10}$$

where $\boldsymbol{B}_t$ is the toroidal component in the toroidal direction and $\boldsymbol{B}_p$ is the poloidal component inside the poloidal plane perpendicular to $\boldsymbol{B}_t$. Define the field angle, θ, as the angle between $\boldsymbol{B}$ and $\boldsymbol{B}_t$. Typically for SOL magnetic field $\boldsymbol{B}_t \gg \boldsymbol{B}_p$ resulting in a very small θ. For a given *poloidal length*, $\triangle l_p$ (the length measured along a flux surface in the poloidal plane), a field line with a smaller θ travels a larger distance around the torus resulting in a larger $\triangle l$. A smaller θ is achieved by reducing $\boldsymbol{B}_p$. If $\boldsymbol{B}_p = 0$, as in the case of an X-point, the field line wraps around the torus forever. Therefore in order to increase L, one can reduce $\boldsymbol{B}_p$ for part of the SOL. An intuitive way to visualize this concept is to use *poloidal flux expansion*, defined as B_p^{-1}. A smaller $\boldsymbol{B}_p$ (smaller θ) means a larger poloidal flux expansion which is indicated by a larger separation between flux surfaces on a 2D plot of the poloidal plane.

The *X-divertor* (XD) reduces $\boldsymbol{B}_p$ by inducing a second axisymmetric X-point downstream of the main plasma X-point [16, 18, 19]. Since $\boldsymbol{B}_p = 0$ at the second X-point, the poloidal flux expansion and the connection length from the main X-point to the target plate are increased (Fig. 2.8).

An ideal *snowflake divertor* reduces $\boldsymbol{B}_p$ by converting the main X-point [24, 25] into a second order null. By making not only the value but also the gradient of $\boldsymbol{B}_p$ zero at the main X-point, snowflake greatly reduces the nearby B_p resulting in a large poloidal flux expansion and effectively increases L near the main X-point (Fig. 2.9).

For both the X and the snowflake divertors, increasing poloidal flux expansion can increase the connection length which will increase the difference between the upstream and downstream T_e ; the impurity radiation is increased as well.

Although it looks like that the separation of flux surfaces are increased a lot due to the increase of poloidal flux expansion, the cross-sectional area of the actual flux tube in 3D space is not expanded much. This is because the fact that $\boldsymbol{B}_t \gg \boldsymbol{B}_p$ and the cross-sectional area, or equivalently the *total flux expansion* B^{-1}, is mostly determined by the strength of the toroidal field. In fact the reduction of the "heat flux" in the XD configuration is simply a reduction of the *perpendicular heat flux*, $Q_\perp$, the perpendicular projection on the target. In this sense, the XD, *inter alia*, does

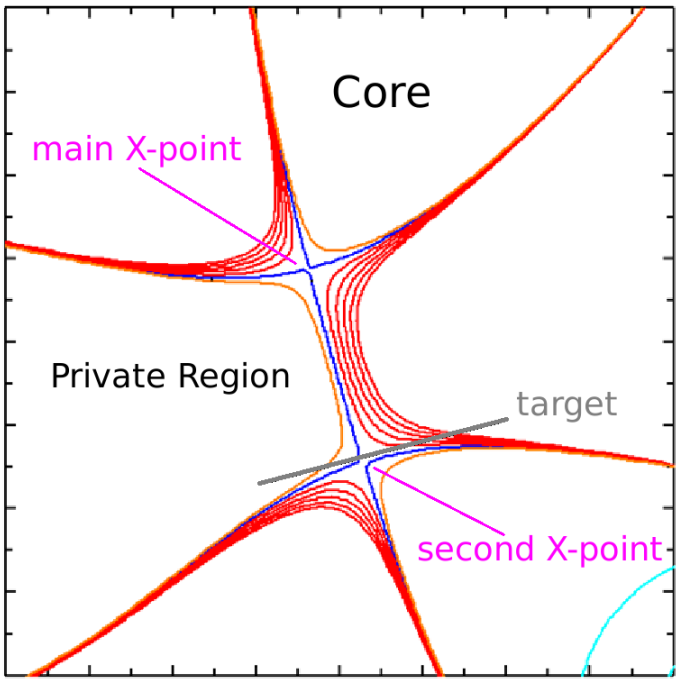

Figure 2.8: An illustration of the concept of X-divertor showing the largely increased poloidal flux expansion near the second X-point.

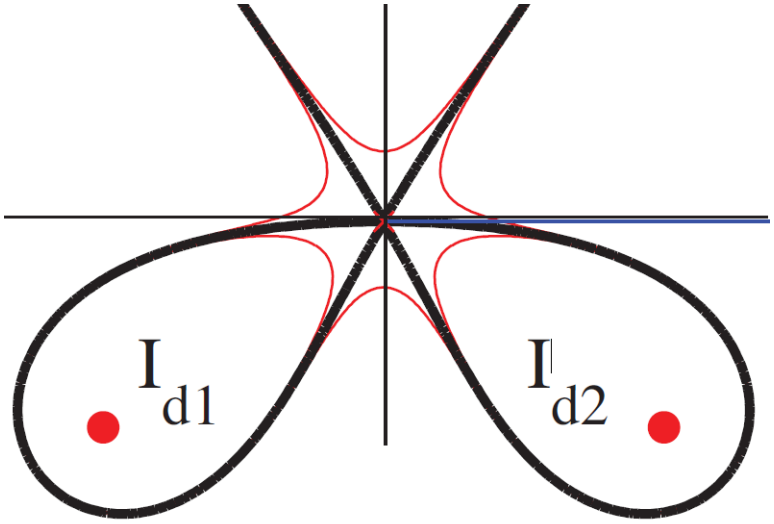

Figure 2.9: An illustration of the second order null of a snowflake divertor. Picture courtesy of D.D. Ryutov [24].

increase the wetted area similar to the tilting of the divertor target as mentioned at the beginning of this section.

If the total flux expansion can be increased, then the total heat flux, or the *parallel heat flux* $Q_{\parallel}$, can be reduced accordingly. If it can be achieved, the benefit for reducing the target heat load is huge and fundamental as is essentially equivalent to increasing the SOL width. To increase total flux expansion, one must increase the dominant *toroidal flux expansion* B_t^{-1}. The toroidal field is mostly determined by the TF coils and varies geometrically as $1/r$, where r is the distance from the center of the tokamak. Therefore increasing toroidal flux expansion means to move the strike point and the target radially out. This is possible and achievable with the *super-X divertor* (SXD) which was invented in 2007 [17, 30, 31, 32]. In an SXD, multiple auxiliary X-points are introduced axisymmetrically to bend the divertor leg in the poloidal plane so as to guide the SOL to the target farther away from the center (Fig. 2.10 and 2.11). In an SXD not only the total flux expansion is increased but the connection length L is also substantially increased due to the elongation of the divertor leg (or SOL).

Despite the additional advantages, super-X divertors need sophisticated PF coils to create and control the X-points, and also take extra space inside the vacuum vessel. Without a change in hardware design, such an option is not available on most of current tokamaks including DIII-D, JET and ITER. However it is quite possible that in future high yield fusion machines, SXD like configurations may become a necessity.

2.2.3 Advanced divertors, regarding SOL detachment

As mentioned in the previous section, since there are practical limits to the lower bound of θ the reduction in perpendicular heat flux by wetted area expansion is fundamentally limited for an attached plasma. The only option left for most of current machines (except those equipped with an SXD) to solve the power exhaust and target erosion problems is divertor detachment.

The energy exchange channels are dissipation channels for the SOL plasma as mentioned in section 2.1. The heat received by the target is reduced when there is

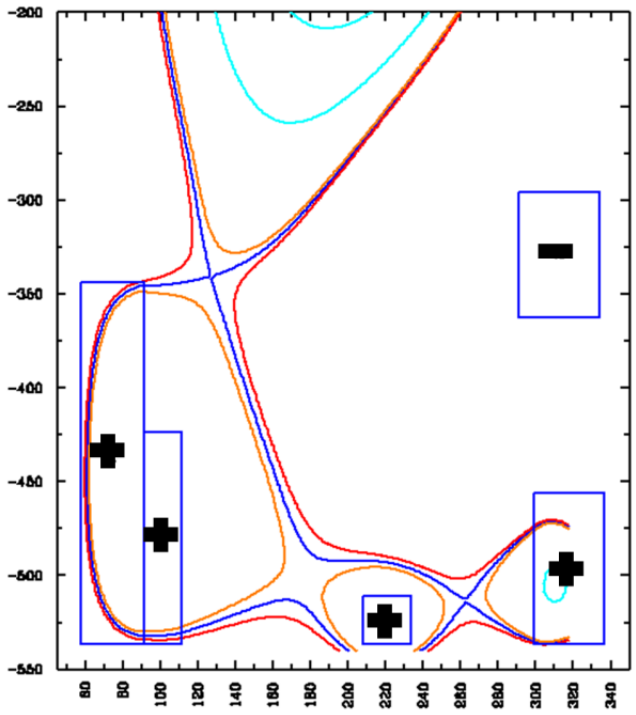

Figure 2.10: By creating multiple new x-points, it's possible to control the path of the divertor leg to increase R of the strike point and create flux expansion, as in the Super X-Divertor design. Figure courtesy of Brent Covele [11].

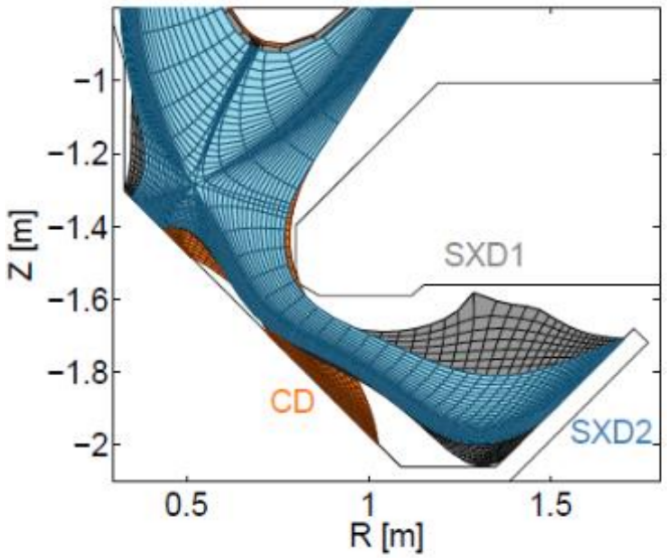

Figure 2.11: Super-X divertors developed on the MAST tokamak. [15]

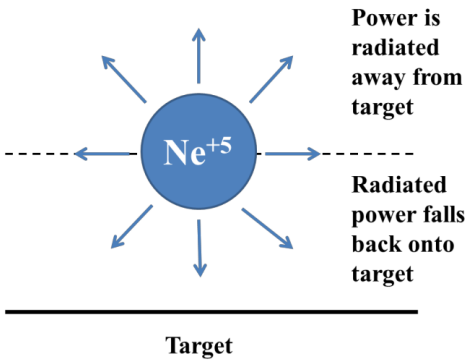

Figure 2.12: Atomic radiation as an example showing that the energy can be carried away from the target by neutrals (photons in this example).

more interaction between plasma particles and impurities(neutral atoms or impurity ions). This is because neutral atoms or photons, do not follow the magnetic field lines and thus they can carry the energy away from the target (Fig. 2.12) reducing target heat load.

At high levels of atomic dissipation, the SOL plasma may manifest *detachment*, that is, a transition from plasma-dominated physics to neutral-dominated physics occurs between the upstream plasma and the material surface. The transition SOL region is known as the *detachment front*. Full detachment creates a neutral buffer layer near the target (Fig. 2.13) and greatly reduces the plasma temperature, pressure and parallel heat flux downstream.

To achieve detachment, the downstream temperature at the target needs to satisfy the condition $T_{e,d} \leq 5\text{eV}$. For a given heat flux $Q_{\|}$ and a given upstream density $n_{e,u}$, $T_{e,d}$ is lower for higher L (Eq. 2.9). Thus there is an apparent benefit on detachment due to increased connection length in the advanced divertor geometries.

When the energy sink term R in equation 2.1 is considered, there is more benefit because of a longer connection length L. The major contribution to R is radiation from partially ionized impurities, which depends on L. The radiated power for a given radiating temperature, $T_e = T_{rad}$, scales as $P_{rad} \sim n_e n_{imp}$ (see Fig. 2.2). As indicated by Eq. 2.6, for a given upstream density, $n_{e,u}$, the longer L is the higher the pressure is. Therefore by $p \sim n_e T_e$, at a any T_{rad}, n_e is higher and hence the radiated power P_{rad} is higher for a longer L.

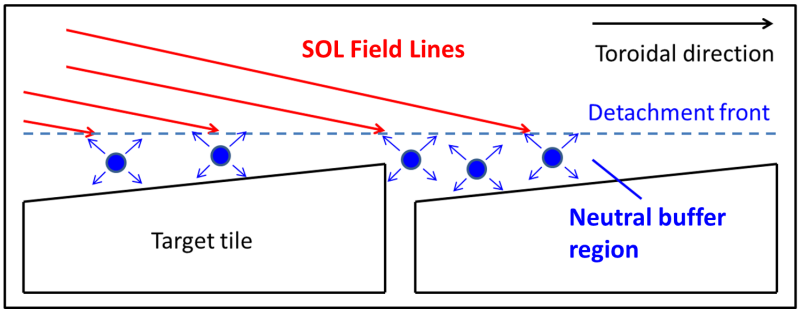

Figure 2.13: A detached SOL solves the heat flux problem by separating the SOL plasma from the targets. The issue of the target angle and hot spot formation also becomes moot, as neutrals in the buffer region are not influenced by magnetic field lines. Figure courtesy of Brent Covele [10].

For a given upstream density, $n_{e,u}$, advanced divertors with longer connection length result in lower $T_{e,d}$ and higher P_{rad} which is more favorable for achieving detachment. In other words, when equipped with an advanced divertor, a tokamak can achieve SOL detachment more "easily" (at a lower $n_{e,u}$ or less neutral gas puff). The less gas puffed into the system, the better preserved is the core confinement.

Detached operation would be highly desirable in order to solve the power exhaust and erosion problems. However, experiments have found that strong detachment often makes the main plasma suffer by degrading H-mode confinement quality or causing disruption. Such drawbacks are suspected to be the results of upstream migration of detachment front (in SD configurations) which brings a cold, highly radiating plasma to the edge of the core. Thus fully detached regime has not been adopted for fusion grade plasmas. If the advanced divertor geometries could enable fully detached operation without degrading the main plasma, the resulting benefits could be enormous.

It is found that XD, or SXD, may be the best candidate to facilitate detached operation in tokamaks:

1) First it has been argued that the increased connection length will achieve SOL detachment more "easily"; this holds for both XD and SXD. The large poloidal flux expansion near the target of an XD brings some extra benefit that comes from plasma -neutral interaction.

It has been pointed out in section 2.1 that energy losses in plasma-neutral and plasma-impurity interaction channels are only significant in the low temperature range

($\sim$ 10eV). A typical T_e profile, in NSTX-U for example, varies from $\sim$70eV upstream to $\sim$2eV downstream and hence the part of SOL with the temperature range for significant plasma-neutral interaction is close to the target. Furthermore, since neutral density is higher near the target, strong plasma-neutral interaction is mostly concentrated in the downstream region close to the target.

Because of a large poloidal flux expansion near the target, the XD distributes a large portion of the connection length downstream near the target where there can be very strong plasma-neutral interactions.

Also, a large poloidal flux expansion means a smaller field angle θ. At a point with a given perpendicular distance away from the wall, a smaller θ means a longer l along the field line between that point and the strike point; that means a higher T_e at that point (Eq. 2.3). Thus a neutral will charge exchange with an ion that has higher energy implying that the energy loss of the plasma due to charge exchange is increased in an XD geometry.

2) Secondly and even more importantly, XD can stabilize the detachment front whereas SD and SFD can not.

To explain this crucial advantage, we must invoke a third geometric characteristic —*poloidal flaring*. There is a key distinction between the divertor geometries: approaching the target from upstream, the SD and SFD field lines converge whereas the XD and SXD field lines diverge because of the secondary X-point near the target. The divergent character of the field lines is known as the poloidal flaring effect: as $\boldsymbol{B}_p$ gets weaker as the target is approached, the total field becomes more and more toroidal, and a field line travels a larger distance around the torus for a given increment of poloidal length.

The degree of plasma-neutral interaction depends largely on the local poloidal flux expansion, or *interaction length*, $\triangle l$, that is the length along the field line for a given poloidal length (or neutral mean free path). Therefore, divergent flux surfaces (the XD) and convergent flux surfaces (SD or highly convergent ones of SFD) will trigger different feedback responses as the detachment front proceeds upstream from the divertor plate toward the main plasma X-point: (1) For an SD or an SFD, the flux expansion increases and $\triangle l$ increases as the detachment front goes upstream. Consequently, the associated energy losses increase. This is a positive feedback that tends to cause a radiation collapse of the front so that it moves even further toward the main plasma X-point. (2) On the other hand an XD or SXD has a uniquely stabilizing

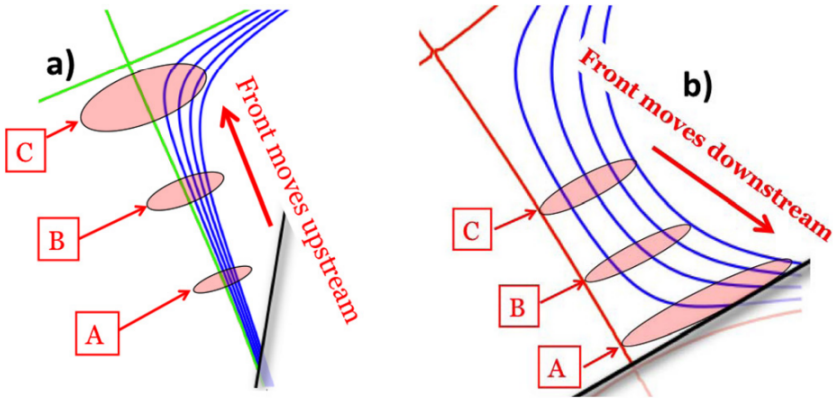

Figure 2.14: SD (a) and XD (b) have opposite feedback effects on detachment front migration. Figure courtesy of Mike Kotschenreuther [20]

feedback in the region of field line flaring, since the flux expansion decreases and $\triangle l$ decreases as the main plasma X-point is approached. Such favorable magnetic geometry tends to localize detachment fronts in the region near the divertor plate retarding movement toward the main plasma X-point. (See Fig. 2.14)

It should be noted that there has not been any theoretical understanding of detachment at a quantitative level because it involves very different fields of physics —plasma transport, neutral transport and atomic physics etc.. Numerical simulations are necessary when studying detachment. The empirical arguments made in this section are also justified with the support of simulation results in section 4.2.

2.2.4 Classification of advanced divertors

A metric that can classify the different divertors is worthwhile. Although the differences in divertor performance arise in the context of plasma-neutral interaction, the differences in the various divertor configurations are geometric in nature. Thus a metric purely based on the magnetic geometry is more intuitive. Yet the differences in divertor performance should also be compatible with the classification by the metric.

It is argued in the previous section that the total connection length L is not a complete metric since it does not tell the difference regarding plasma-neutral interaction. Instead the connection length distribution is a good candidate. A proper metric should reflect the flaring effect which is the unique geometric characteristic of an XD.

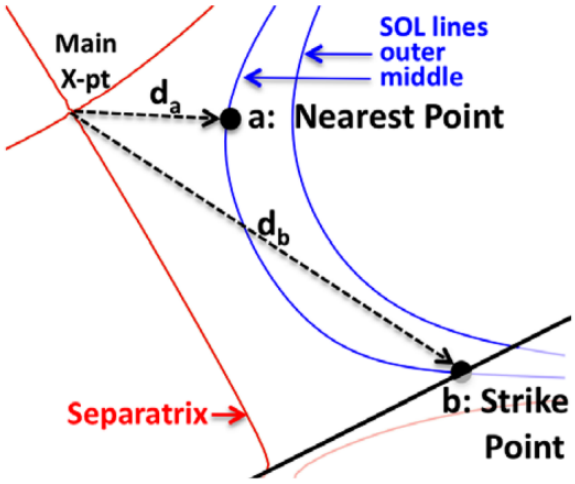

Figure 2.15: SOL geometry for calculation of DI_{SOL}.

The *divertor index*, DI, developed by the University of Texas group [20] , is a simple number that reflects the differences in connection length distribution. In developing DI, the standard divertor provides the fiducial reference. For example, the XD is differentiated from an SFD because the former (latter) has flux surfaces that are more divergent (convergent) than the SD. "Convergence" of flux surfaces relative to a Standard Divertor, may be measured by what has been called, the SOL Divertor Index:

$$DI_{SOL} \equiv \frac{d_b/B_{p,b}}{d_a/B_{p,a}} = \frac{B_{p,a}}{B_{p,b}}\frac{d_b}{d_a} \tag{2.11}$$

where d is the distance of a point from the main X-point and B_p is the poloidal magnetic field strength, a is the point on a representative flux surface that are closest to the main X-point upstream and b is the strike point of that flux surface (Fig. 2.15). If $DI_{SOL} > 1$, the flux surfaces are more flared than an SD, and if $DI_{SOL} < 1$, it is more contracting than an SD.

An alternative quantity DI, which is somewhat simpler to compute in practice, may prove more useful. Since point a is near the main X-point, we can use the approximation $B_{p,a}/d_a \longrightarrow |\nabla B_{p,X}|$ to define

$$DI \equiv |\nabla B_{p,X}|\,\frac{d_b}{B_{p,b}}. \tag{2.12}$$

For a Standard Divertor, $DI = 1$. For a pure Snowflake, $DI = 0$ since the gradient of

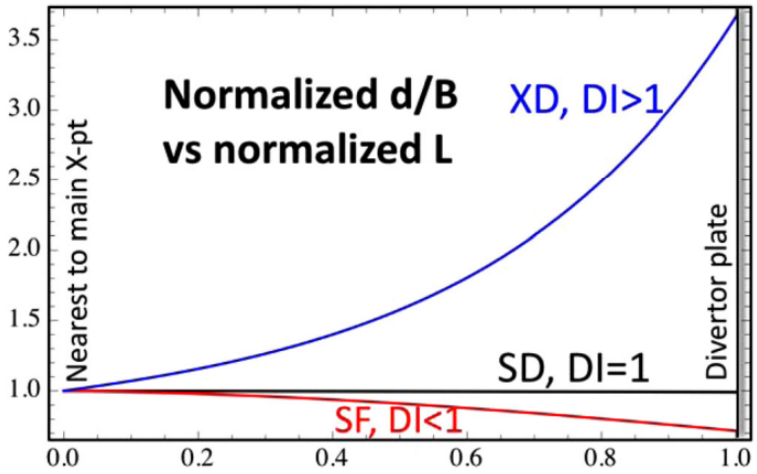

Figure 2.16: Plots of d/B_p vs normalized distance l^* along the field line starting from a point nearest to the main X-point ($l^* = 0$) to the strike point ($l^* = 1$). Figure courtesy of Mike Kotschenreuther [20]

B_p is zero at the main X-point. For a "pure" XD where the second X-point is located at the strike point, DI approaches infinity. Fig. 2.16 shows a typical profile of DI for the three different divertors from the main X-point to the strike point. It can be seen clearly that the three are distinct and well separated.

Before wrapping up this section, it is worth mentioning that a type of divertor, called *Cusp Divertor*, is very similar (in some aspects) to the XD family. A cusp divertor creates a second X-point (a cusp) using four symmetric coils near the target (Fig. 2.17). It has the flaring effect that an XD has. However, there is a qualitative difference in divertor $\boldsymbol{B}_p$ between an XD and a cusp divertor. In an XD, a dipole-like poloidal field is introduced against the original $\boldsymbol{B}_p$ of an SD to create the second X-point and hence the original $\boldsymbol{B}_p$ is weakened thourghout the entire divertor leg. By contrast, in a cusp divertor the quadrupole-like poloidal field created by the four coils is, for most part of the divertor leg, in the same direction as the original $\boldsymbol{B}_p$ of an SD and thus enhances the original $\boldsymbol{B}_p$. The poloidal field B_p is much stronger in a cusp divertor as it goes upstream away from the second X-point. Thus the connection length of a cusp should be shorter than an XD, even though the flaring can be similar. Simulations of the cusp geometry, compared to a similarly flared XD, could be used in the future to help determine the relative importance of flaring and connection length

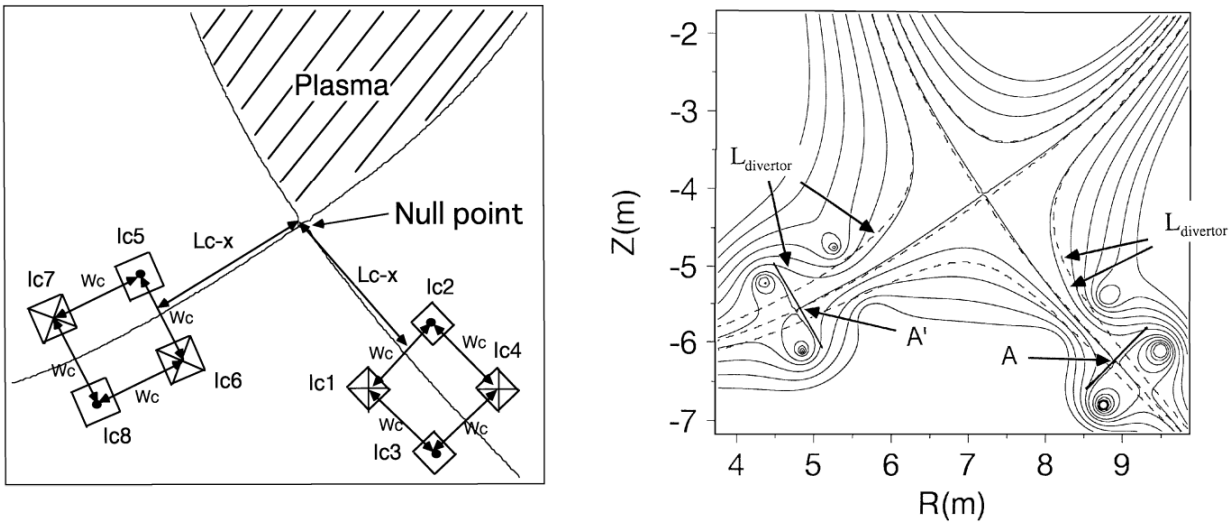

Figure 2.17: Illustrations of the four PF coils used to generate a cusp (left) and the flux surfaces of a cusp divertor (right). Figure courtesy of Haruhiko Takase [29].

in divertor performance. The divertor index, DI, may not be enough to differentiate an XD from a cusp. Thus an auxiliary metric is currently under development. Some intuitive arguments will also be given in section 3.2.

Chapter 3

Geometric Modeling of Divertors

In this chapter, various divertor configurations are constructed using the magnetic equilibrium code CORSICA [12]. In the first section, various advanced divertors, generated for NSTX-U, are presented and their properties are compared from purely geometrical points of view. The comparison involving SOL physics (with supporting evidence from simulations) for two of the representative divertors will be presented in chapter 4. In Section 3.2, the SD, XD and the cusp, generated on ITER, are compared and a way to differentiate XD from the cusp is proposed.

The details about the equilibrium code CORSICA are given in appendix B.

3.1 Advanced divertors on NSTX-U

The National Spherical Torus Experiment (NSTX) at the Princeton Plasma Physics Laboratory has been recently upgraded. The upgraded machine, the NSTX-U, is the premiere low-aspect ratio tokamak in the United States. Following the very successful run of NSTX, several major updates have been implemented so that NSTX-U may serve as a precursor to a Fusion Nuclear Science Facility (FNSF). Significant changes include a doubling of the plasma current, toroidal field, and neutral beam heating power, as well as increasing the plasma pulse length from 1-1.5 seconds to 5-8 seconds [21].

Various X-divertor configurations have been developed on NSTX-U using CORSICA. The PF coil set (Fig. 3.1) and the current limits are the major challenge for changing the magnetic equilibrium to make advanced divertors. The required plasma properties for stability purposes also made it harder when the equilibria were developed. Despite these difficulties, is has been possible to create X-divertors respecting all the machine/physics constraints.

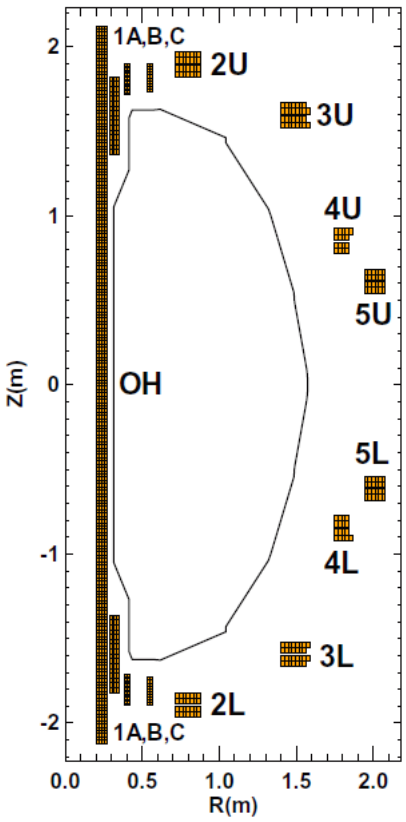

Figure 3.1: The PF coil set and solenoid for NSTX-U. [13]

3.1.1 The SD and the XD

In order to demonstrate the advantages of the XD over the SD, we must create and investigate the two configurations keeping the same core plasma properties; the differences in the SOL properties, then, will reflect only the effects of the different divertor geometries. We were, indeed, able to follow this prescription. In fact, the modification to the magnetic geometry in the divertor region downstream did not perturb the core plasma much. The core shapes for the two cases are almost the same with very similar main X-point locations (Fig. 3.2). Some of the key parameters of the core plasma properties are compared in Tab. 3.1, from which it can be seen that the two equilibria indeed share similar core properties.

The PF coil currents used to generate the XD case are displayed in Tab. 3.2; the relevant currents for SD are mostly similar except the ones for divertor control (the latter do not affect the core by much).

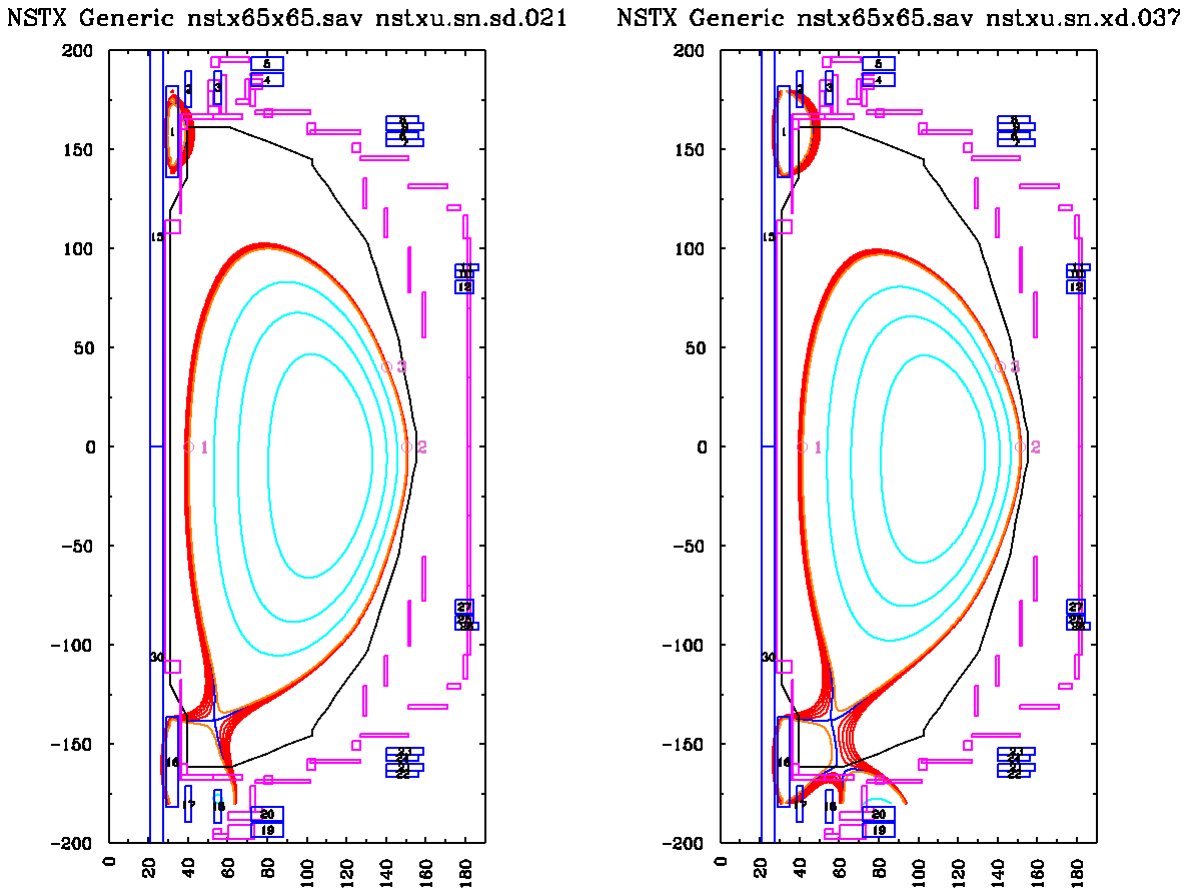

Figure 3.2: A comparison of the free-boundary magnetic equilibria with an SD (left) and the XD (right).

The outer divertor regions of the SD and XD geometries, displayed in Fig. 3.3, also show the key distinctions between them: approaching the target from upstream, the SD field lines converge whereas the XD field lines diverge because of the second X-point. The XD has a $DI = 26.6$ with highly divergent flux surfaces showing a substantial poloidal flaring (section 2.2.3).

The contracting flux surfaces of the SD result from the increase in B_p towards the target. As a result the field angle θ gets steeper. On the contrary, the flared flux surfaces of the XD result in a shallower total field angle when it approaches the target downstream as shown in Fig 3.4. Since the downstream total magnetic field becomes more and more toroidal, the field lines of the XD travel larger distances around the

	SD	XD
I_{plasma}, B_{tor}	1.103, 0.742	1.107, 0.735
R, a, R/a	0.953, 0.551, 1.729	0.963, 0.550, 1.749
β_{norm}	4.387	4.671
q_{95}	6.099	5.566
elongation 95(edge)	2.068 (2.168)	1.993 (2.124)
U. triangularity 95(edge)	0.260 (0.278)	0.269 (0.289)
L. triangularity 95(edge)	0.475 (0.733)	0.468 (0.665)

Table 3.1: A comparison of the core plasma properties of the magnetic equilibria with an SD and the XD.

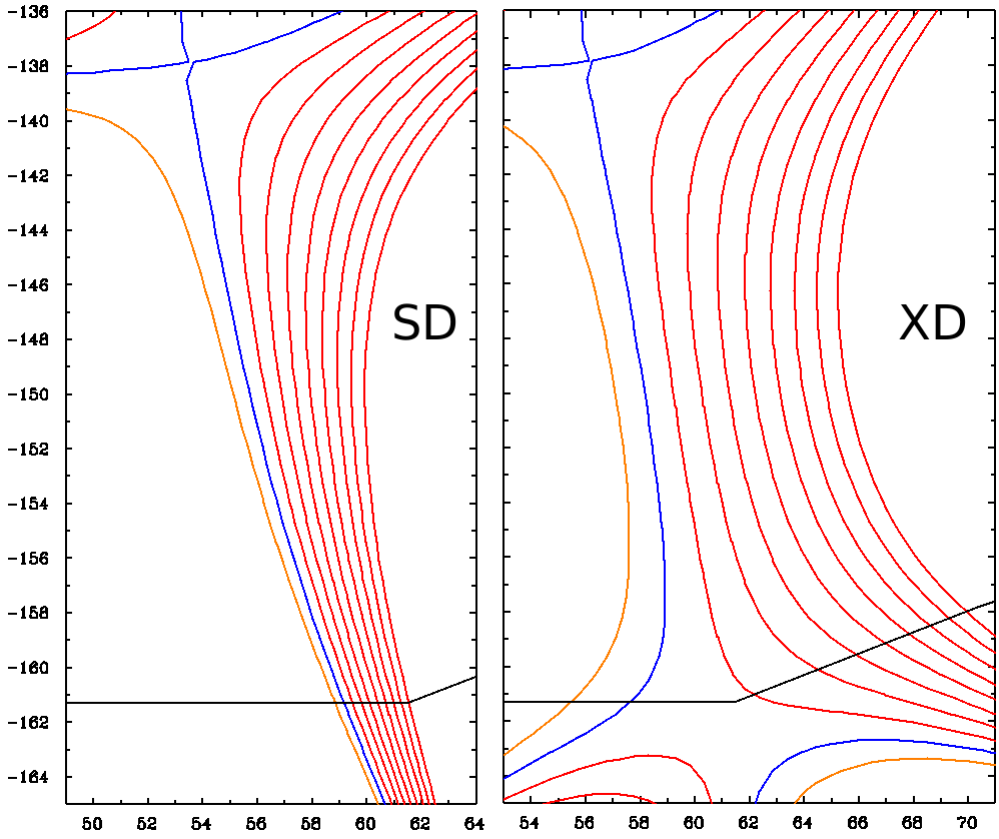

Figure 3.3: Comparison of the SD (left) and XD (right) geometries. The adjacent SOL flux surfaces are 0.5 mm apart at the outboard midplane.

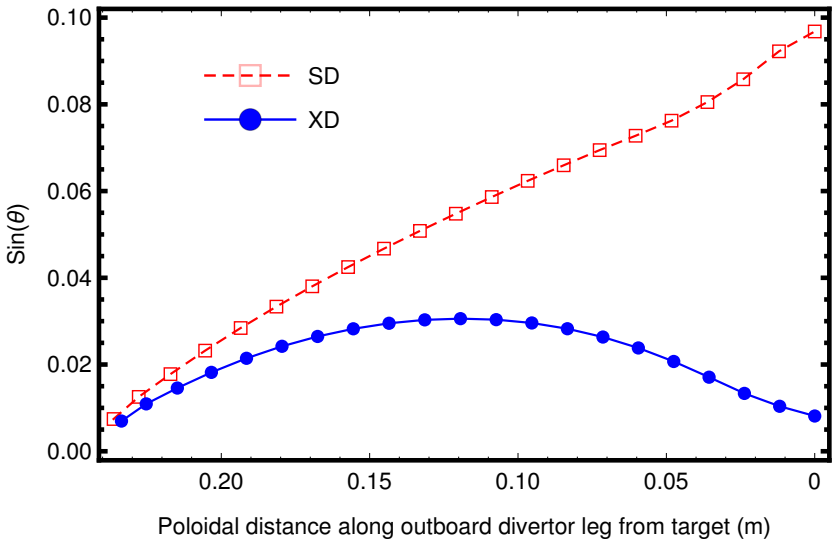

Figure 3.4: Comparison of the angle θ between the total field and the toroidal direction from upstream to downstream along the SD and XD divertor legs. The SOL flux surfaces are 0.3mm from the the respective separatrices at the outboard midplane. The horizontal axis represents the poloidal distance from a given point on the flux surface to the target, the distance measured along the flux surface in the 2D poloidal plane, not distance along the field line in 3D space.

torus for the same increment of poloidal length. Consequently a large portion of the connection length of the XD is distributed in the neutral dense region near the target where the collisionality with neutrals is the strongest (see Fig. 3.5). In other words the XD has a larger interaction length $\triangle l$.

The poloidal flaring of the XD is not restricted to any particular flux surface; instead, it is consistent across the entire target in the radial direction. This can also be seen from a comparison of the incident angles of the SD and XD cases across the wetted area (Fig. 3.6).

Such geometric effect of the XD facilitates an easier and more stable detachment to be demonstrated in chapter 4.

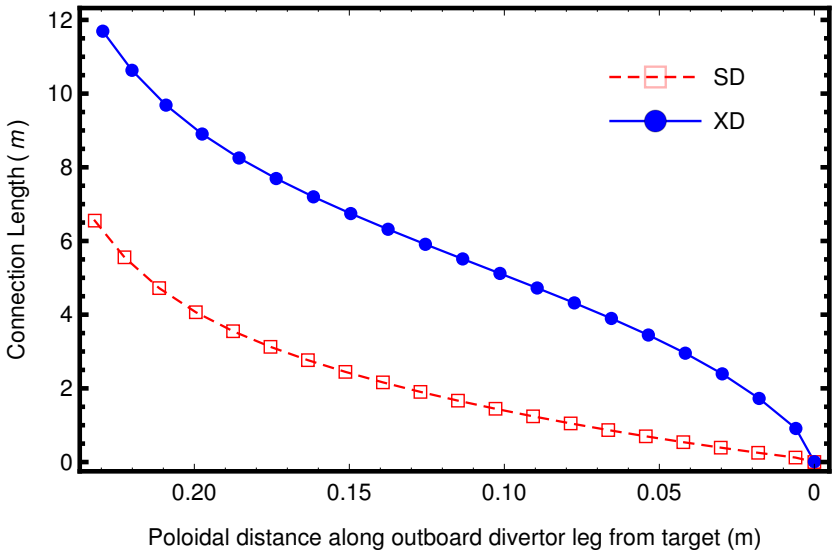

Figure 3.5: Comparison of the connection length distribution from upstream to downstream along the SD and XD divertor legs. Here, connection length is defined as the distance along a flux surface from the target to the poloidal distance from the target plotted on the X-axis. The SOL flux surfaces are 0.3mm from the the respective separatrices at the outboard midplane.

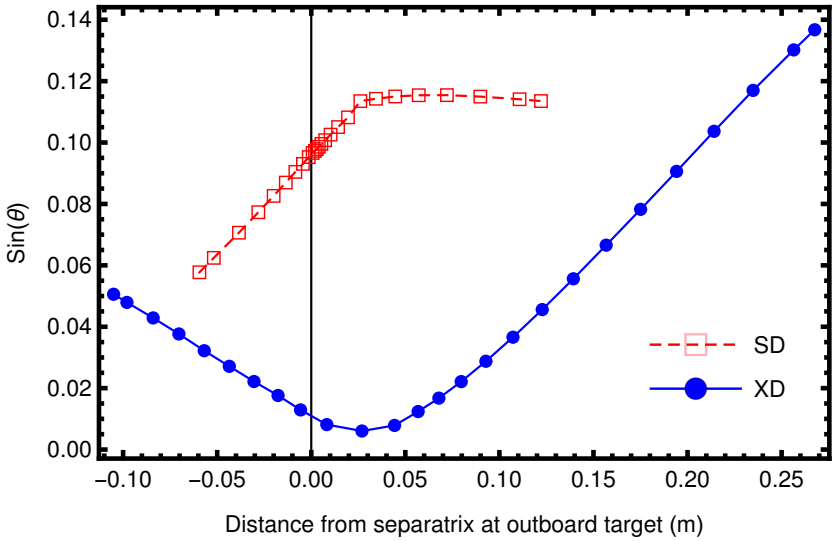

Figure 3.6: The radial profiles of the incident angle θ at outboard target for the SD and XD cases.

3.1.2 Other XD's

The XD shown above is the best one (with the highest divertor index) we have been able to construct. Notice that, in experiment, it is not always possible to measure all the "good" properties of the magnetic geometry. This is because the experimental diagnostics are fixed in space and each of them has a finite domain in the vacuum vessel where the resolution is satisfactory. Use Thompson scattering as an illustrative example. (NSTX-U does not have a divertor Thompson system, other tokamaks do.) Though Thompson scattering is a great tool for measuring temperature, it can, in general, measure only at a collection of locations along a line rather than a finite domain. Thus measuring a 2D temperature profile for the whole divertor region is impossible. What is worse is that, sometimes, the line of Thompson scattering measurement covers the least important part of the divertor leg. In situations like such, it is not practical (and often impossible) to make hardware change to the diagnostics since they have already been built in the machine. Therefore, the only option for divertor designers is to change the divertor geometry, more specifically to sweep the divertor leg.

Ideally, one can sweep the divertor leg by moving the location of the second X-point of the XD. However in practice it turns out to be difficult. With the NSTX-U coil set, one does not have a luxury set of PF coils to control the second X-point; the PF1c and PF2 are the only relevant coils. The attempt at moving the second X-point location in the radial direction along the target by manipulating the PF1c and PF2 coil currents (Tab. 3.2) did not succeed.

Yet fortunately, instead of the second X-point, the strike point moves when the PF1c and PF2 coil currents change. This effectively sweeps the divertor leg. A full control of the strike point location is possible with the coil set. Shown in Fig. 3.7 are two cases with the strike point location radially inner and outer as compared with the best XD respectively.

Although moving the second X-point radially is impossible with the coil set, it is not too hard to move it downward along the divertor leg. As the second X-point is moved away from the target (the strike point), the poloidal flaring gets weakened and the divertor index decreases. Two of such cases are shown in Fig. 3.8. If the second X-point is moved infinitely far away from the main X-point, then the XD becomes an

#	Name	ic	wgt(svec)	I(MA)	rc	zc	drc	dzc	nrc	nzc	MA/m2	MW
1	PF1a	1	1.0d+00	0.423	0.319	1.591	0.061	0.458	1	10	15.252	0.518
2	PF1b	0	1.0d+00	0.000	0.400	1.804	0.034	0.181	2	2	0.000	0.000
3	PF1c	0	1.0d+00	0.000	0.550	1.814	0.037	0.166	2	2	0.000	0.000
4	PF2a	2	1.0d+00	0.042	0.799	1.853	0.163	0.068	3	1	3.813	0.032
5	PF2b	2	1.0d+00	0.042	0.799	1.933	0.163	0.068	3	1	3.813	0.032
6	PF3a	3	1.0d+00	-0.047	1.483	1.570	0.163	0.034	1	1	-8.546	0.151
7	PF3b	3	1.0d+00	-0.047	1.494	1.536	0.186	0.034	1	1	-7.478	0.133
8	PF3c	3	1.0d+00	-0.047	1.483	1.651	0.163	0.034	1	1	-8.546	0.151
9	PF3d	3	1.0d+00	-0.047	1.494	1.617	0.186	0.034	1	1	-7.478	0.133
10	PF4a	0	1.0d+00	-0.000	1.795	0.871	0.092	0.034	2	1	-0.000	0.000
11	PF4b	0	1.0d+00	-0.000	1.806	0.905	0.115	0.034	2	1	-0.000	0.000
12	PF4c	0	1.0d+00	-0.000	1.795	0.807	0.091	0.068	2	1	-0.000	0.000
13	PF5a	4	1.0d+00	-0.142	2.012	0.649	0.136	0.069	2	1	-15.290	1.100
14	PF5b	4	1.0d+00	-0.142	2.012	0.575	0.136	0.069	2	1	-15.290	1.100
15	OH	0	1.0d+00	0.000	0.242	1.060	0.069	2.121	1	40	0.000	0.000
16	PF1a	0	1.0d+00	0.390	0.319	-1.591	0.061	0.458	1	10	14.058	0.440
17	PF1b	0	1.0d+00	0.000	0.400	-1.804	0.034	0.181	2	2	0.000	0.000
18	PF1c	0	1.0d+00	-0.077	0.550	-1.814	0.037	0.166	2	2	-12.406	0.132
19	PF2a	0	1.0d+00	0.125	0.799	-1.933	0.163	0.068	3	1	11.298	0.284
20	PF2b	0	1.0d+00	0.125	0.799	-1.853	0.163	0.068	3	1	11.298	0.284
21	PF3a	5	1.0d+00	-0.068	1.494	-1.617	0.186	0.034	1	1	-10.656	0.270
22	PF3b	5	1.0d+00	-0.068	1.483	-1.651	0.163	0.034	1	1	-12.178	0.307
23	PF3c	5	1.0d+00	-0.068	1.494	-1.536	0.186	0.034	1	1	-10.656	0.270
24	PF3d	5	1.0d+00	-0.068	1.483	-1.570	0.163	0.034	1	1	-12.178	0.307
25	PF4a	0	1.0d+00	-0.000	1.795	-0.871	0.092	0.034	2	1	-0.000	0.000
26	PF4b	0	1.0d+00	-0.000	1.806	-0.905	0.115	0.034	2	1	-0.000	0.000
27	PF4c	0	1.0d+00	-0.000	1.795	-0.807	0.091	0.068	2	1	-0.000	0.000
28	PF5a	4	1.0d+00	-0.142	2.012	-0.649	0.136	0.069	2	1	-15.290	1.100
29	PF5b	4	1.0d+00	-0.142	2.012	-0.575	0.136	0.069	2	1	-15.290	1.100
30	OH	0	1.0d+00	0.000	0.242	-1.060	0.069	2.121	1	40	0.000	0.000

Total PF power = 7.845 MW, Total PF MA-m = 6.644 = 0.85 times Plasma MA-m = 7.800

TF cur = 3.536 MA, 11.489 MA/m2; B= 2.259 at rTF = 0.313

Table 3.2: A set of PF coil currents used when generating the XD equilibria. The two PF1a coils (in the blue boxes) are the dominant ones controlling the main X-point location. The PF1c and PF2 coils (in the red box) are the most important in controlling the geometry around the second X-point.

SD.

3.2 Cusp divertor on ITER

The X-divertors and cusp divertors, though both have poloidal flaring (section 2.2.4), are readily differentiated. According to the original Takase design, a cusp divertor is generated by introducing an X-point, a cusp in the magnetic field, using four symmetric coils near the divertor target (Fig. 2.17). Although the flux surfaces near the second X-point look similar to the ones of an XD, the natures of the poloidal magnetic fields are different. The poloidal field of a cusp generated by four coils has the characteristic of a quadrupole field that is as it goes away from the cusp towards the main X-point the added quadrupole field is in the same direction as the original $\boldsymbol{B}_p$. By contrast in an XD, since the second X-point is generated by a pair of PF coils outside the vessel, the poloidal field near the second X-point is generally dipole-like

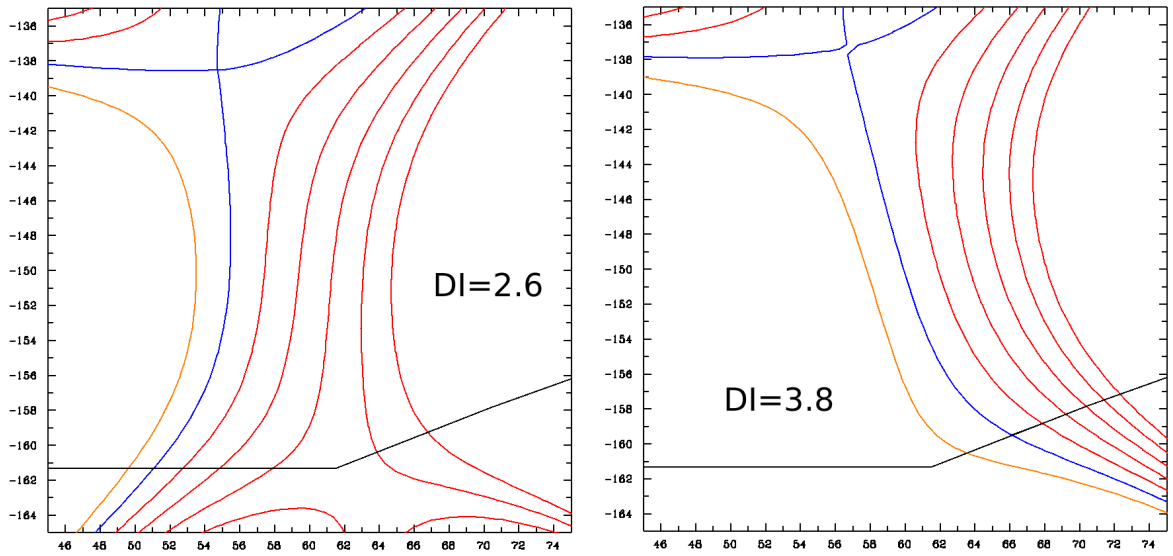

Figure 3.7: Sweep the divertor leg by moving the strike point location along the divertor plate is possible. Therefore diagnostic positions can be accommodated. On the left the X-point is still in the SOL but farther away from the separatrix. On the right, the X-point is in the private region. As the leg is swept, the divertor index changes accordingly.

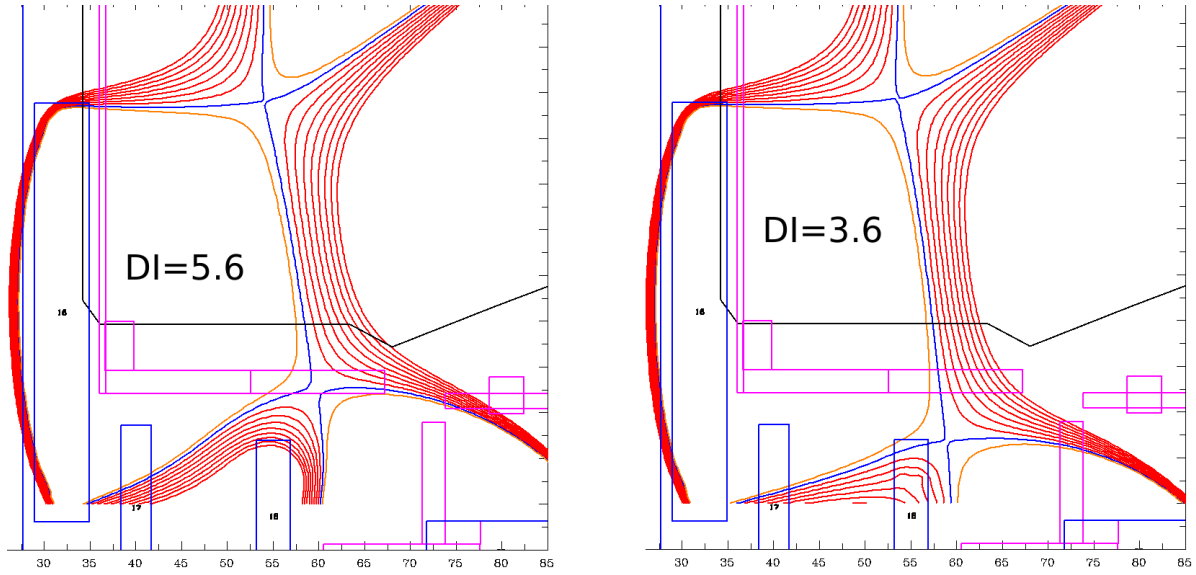

Figure 3.8: XDs with the second X-point 5cm (left) and 10cm (right) down from the strike point. The divertor index decreases. These can serve as comparison cases to the optimal X-divertor to demonstrate the importance of flaring effect.

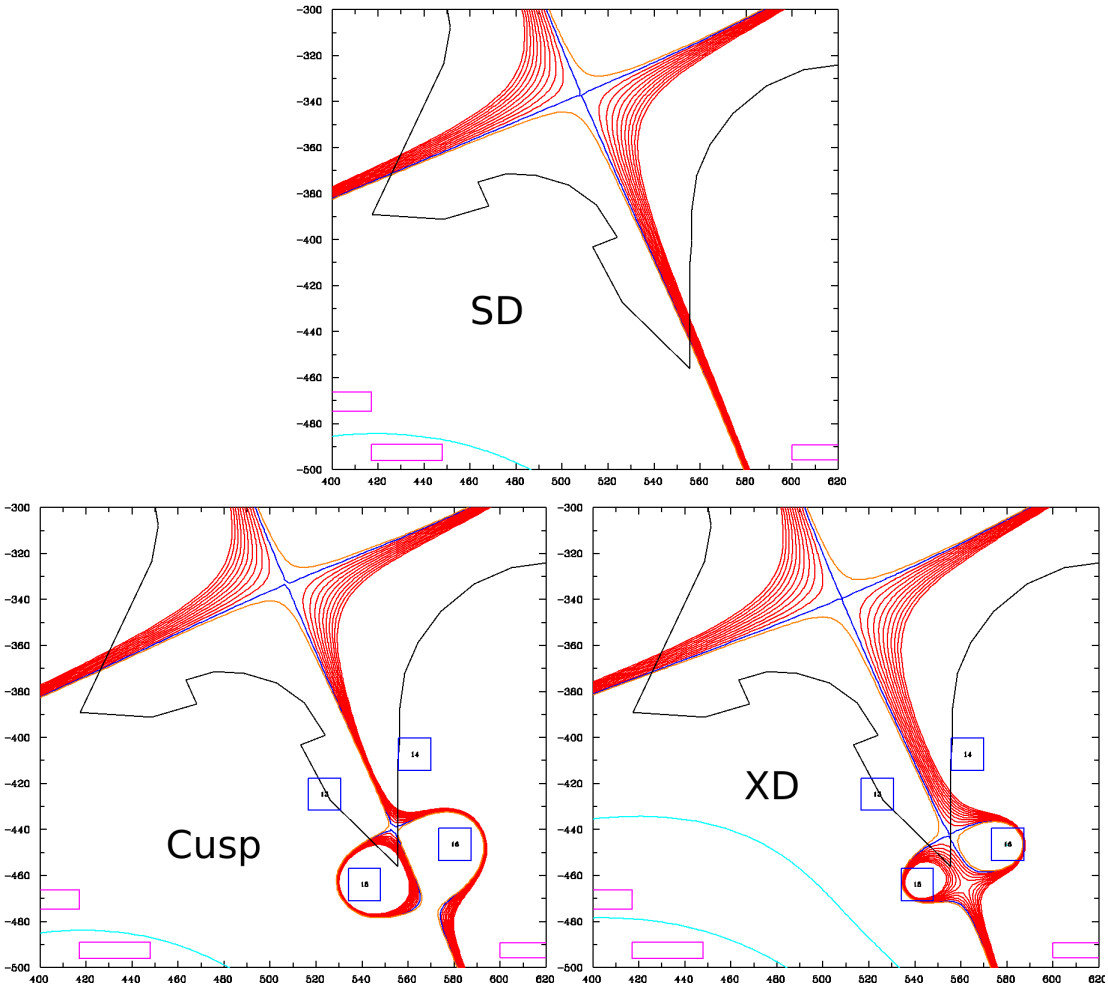

Figure 3.9: A comparison of an SD, a cusp and an XD on ITER.

and is always in the opposite direction to the original $\boldsymbol{B}_p$. Therefore, the B_p along the divertor leg of a cusp divertor is stronger than that of an XD and in fact also stronger than that of an SD. In terms of poloidal flux expansion, the cusp has a smaller flux expansion upstream of the strike point than the SD whereas the XD has a larger one than the SD.

Fig. 3.9 shows a cusp on ITER. It is generated by four PF coils that are not practical for the ITER design. Two of the coils had to be placed inside the vacuum vessel. An XD can also be generated by using only the outer two of these four coils. A comparison with the SD can tell the difference between the cusp and the XD. Although a large poloidal flux expansion is introduced near the target, the flux

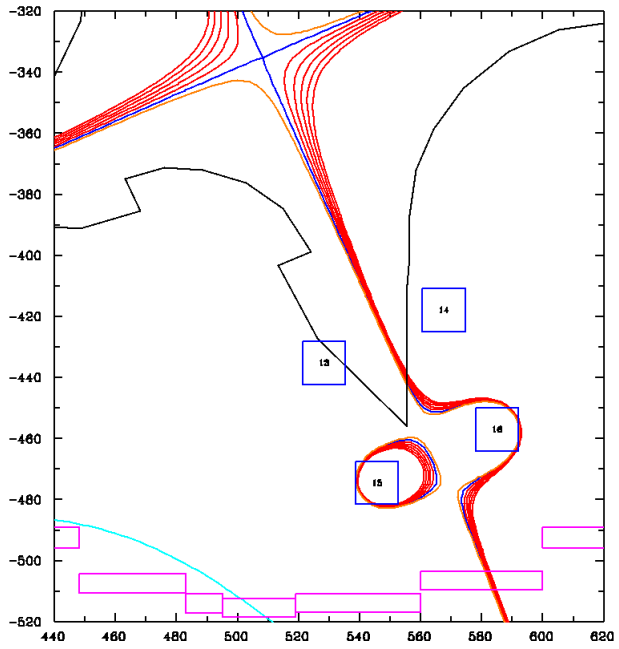

Figure 3.10: Moving the four coils in an asymmetric way destroys the cusp magnetic field.

surfaces pertaining to a large part of the divertor leg upstream are squeezed by the two coils inside the vacuum vessel, resulting in a smaller poloidal flux expansion than the SD. On the other hand, the XD does the opposite: the poloidal flux expansion is bigger than the SD along the entire divertor leg. As discussed in section 2.2.2, poloidal flux expansion determines the connection length and connection length affects divertor performance. The cusp divertor will have a similar connection length as the SD whereas the XD can have a connection length twice as long. Therefore, it is expected that the XD will have a better divertor performance than the cusp divertor. More extensive studies using simulations will be done in the future.

A final remark. It is found that the cusp magnetic geometry is very sensitive to the coil locations. The four coils have to be on the corners of a square and the two sides of the square have to be perpendicular to the divertor leg. If the coils are moved a little and no longer symmetric then the separatrix will not go through the second X-point no matter how the four coil currents are tuned (Fig. 3.10).

Chapter 4

Transport Simulation of Divertors

In previous chapters, different divertors have been compared from a geometrical point of view. It has also been argued, using simple SOL physics, that the difference in divertor geometry makes a difference in actual divertor performance in terms of handling tokamak exhaust problems. The SOL physics, extremely complicated as it is, cannot be meaningfully analyzed analytically. Instead, one has to resort to numerical simulations using sophisticated codes and powerful computers. SOLPS is, perhaps, the most advanced code available for modeling SOL physics and I have heavily used it for divertor studies.

SOLPS simulations for the SD and XD on NSTX-U (presented in section 3.1.1) are presented in this chapter. In the first section, the SD and the XD are compared at the same upstream condition (midplane plasma density at the separatrix) so as to demonstrate that the divertor geometry can greatly affect the downstream SOL properties. Then in the second section, the two divertors are compared in terms of facilitating SOL detachment and stabilizing the detachment front. In the last section, some remarks regarding SOL physics are pointed out.

The series of simulations were conducted in the fashion of a gas-puff scan in order to study the behavior of detachment. Key simulation parameters are: a 3 MW total input power across the core boundary, equally shared between ions and electrons, a constant-particle-flux (zero flux) condition enforced at the core boundary, and constant anomalous radial heat and density-driven particle diffusion coefficients, $X = 0.5$ and $D = 0.15$, to simulate a narrow, H-mode-like power SOL width – about 3 mm. An external constant D_2 gas puff was introduced from far upstream and a weak pumping surface near the outboard target was used to achieve global particle balance. These simulation conditions ensured stable, steady-state conditions at the boundary, while also allowed the core density to evolve in response to the neutral fueling. The technical details of SOLPS code relevant to this research are covered in

Appendix C.

4.1 Advantages of XD on exhaust problem

In this section, SOLPS simulations of the SD and the XD cases are compared assuming similar upstream SOL conditions, more specifically similar separatrix plasma densities at outboard midplane, $n_{e,sep}$. Upstream SOL conditions can be viewed as the boundary condition for the pedestal. Thus similar upstream SOL conditions lead to similar pedestal properties and hence similar core confinement. By comparing the downstream SOL properties while keeping similar upstream conditions, the advantages of XD on tokamak exhaust problems can be clearly demonstrated. It is worth emphasizing that such comparisons make sense only when the two equilibria share similar core shapes. Thus pursuing similar core magnetic geometries while generating different divertors as mentioned in section 3.1.1 is important.

In SOLPS, $n_{e,sep}$ is not a control parameter. However, it can be related to the gas-puff rate which can be controlled. The exact relation between $n_{e,sep}$ and the gas-puff rate depends on the specific divertor geometry. Therefore to make a comparison of the SD and the XD with the same $n_{e,sep}$, a series of parallel simulations with an extensive gas-puff scan is necessary. In this section, the two cases are compared at $n_{e,sep} \sim 3.3 \times 10^{19}\mathrm{m}^{-3}$.

First the poloidal plasma temperature (T_e) profiles along the divertor leg are compared in Fig. 4.1. While the upstream temperatures are similar, the downstream temperature at the target in the XD is significantly lower than in the SD. Thus the XD can lower the down stream T_e while still keep the upstream T_e high, achieving the goal mentioned in section 2.2.1.

The poloidal T_e profiles shown in Fig. 4.1 are only at one flux surface very close to the separatrix. To make it more convincing, the radial T_e profiles along the target is compared in Fig. 4.2. It can be clearly seen that the downstream T_e in the XD geometry is lower than SD across the entire wetted area.

A comparison of the target plasma pressure profile (Fig. 4.3) indicates that the XD has lower peak pressure than the SD. This is because at such upstream conditions the XD SOL has detached while the SD SOL has not. Detachment will be discussed

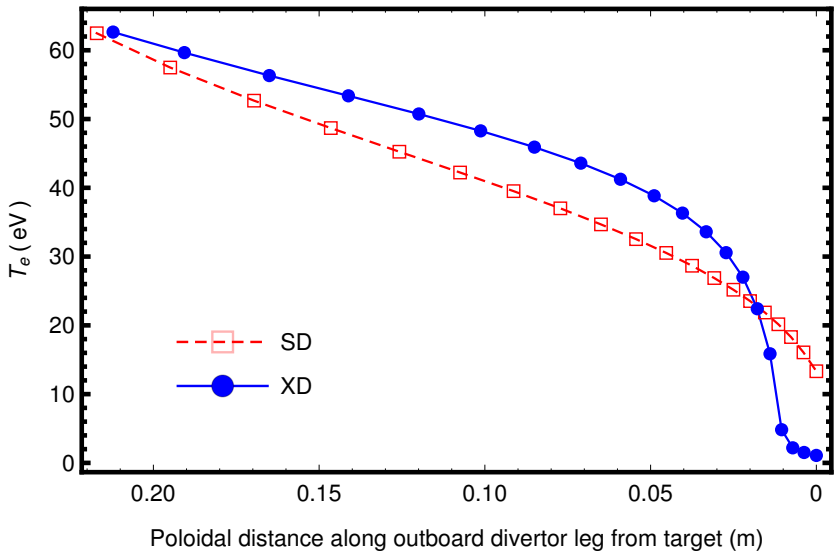

Figure 4.1: The poloidal temperature profiles for the SD and XD cases. The flux surfaces for these 1D profiles were chosen based on the location of the peak values at the divertor entrance.

in the next section.

Next the perpendicular heat flux ($Q_\perp$) profiles along the divertor target are compared (Fig. 4.4). $Q_\perp$ is of key importance in tokamak engineering since the core heating power is limited by the maximum $Q_\perp$ that a target material can handle. One goal of advanced divertor designing is to solve the power exhaust problem by reducing $Q_\perp$ at the target; the XD does it much better than the SD.

The advantage of the XD on reducing $Q_\perp$ is partially due to the much larger poloidal flux expansion that spreads the heat over a larger wetted area (see section 2.2.2). The more important reason is that the power loss due to radiation is higher because of the longer L (section 2.2.3). Also a larger part of the connection length is distributed in the neutral-dense region near the target (see Fig. 3.5). The increased interaction length, $\triangle l$, in this region largely increases the chance of plasma-neutral interactions which are energy loss processes (section 2.2.3). As a result of such increased cooling, the total heat flux $Q_\parallel$ is reduced (Fig. 4.5). Note that $Q_\perp$ is the projection of $Q_\parallel$ on the target.

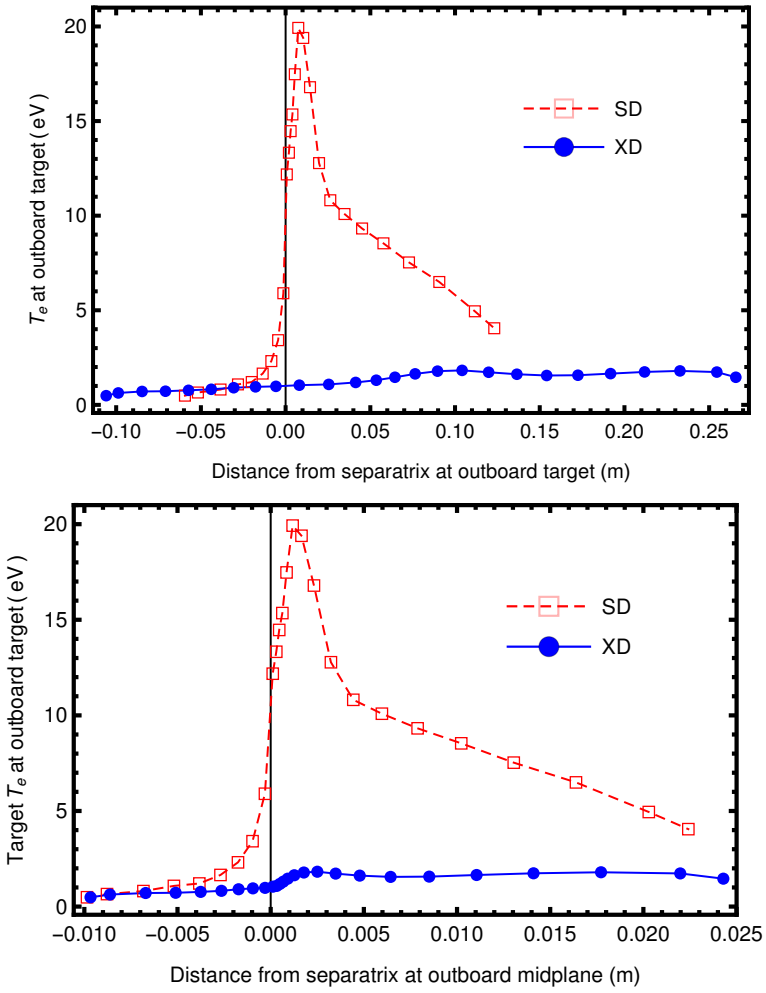

Figure 4.2: The radial profiles of T_e at outboard target for the SD and XD cases. The top graph is plotted against the distance at the target surface and the bottom graph is the same data plotted against the distance at midplane (the same for Figures 4.3, 4.4, 4.5, 4.6 and 4.7).

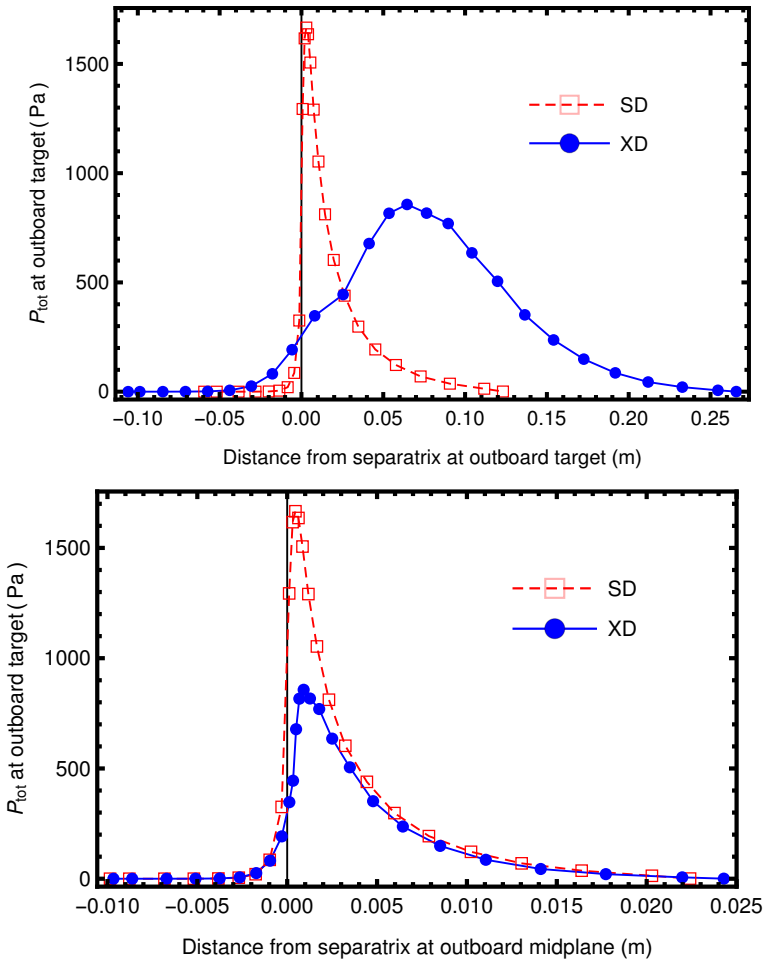

Figure 4.3: The radial profiles of total plasma pressure at outboard target for the SD and XD cases.

Finally, the XD has also demonstrated a reduced ion flux perpendicular to the target (Fig. 4.6). Reduced ion flux means an increase in the target lifetime via reduced sputtering/erosion of the target; the impurity level in the core is, commensurately, reduced.

The reduction of $J_{ion,\perp}$ in this case is mostly due to the increased flux expansion of the XD near the target. There is no significant reduction in the (peak) total ion flux, or $J_{ion,\parallel}$(Fig. 4.7). The total ion flow (integration of the curves in the top graph in Fig. 4.7) is in fact higher for the XD case. This is because a higher gas-puff rate has to be employed in the XD case to maintain the similar $n_{e,sep}$ to the SD case.

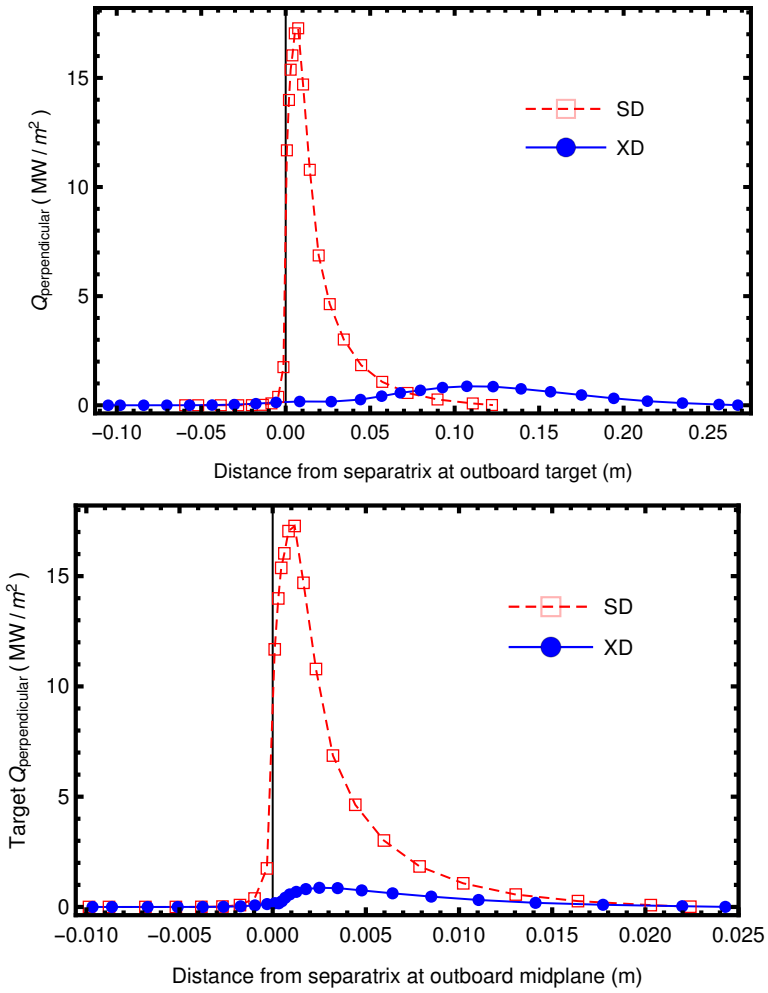

Figure 4.4: The radial profiles of $Q_\perp$ at outboard target for the SD and XD cases.

The reason for a higher gas-puff rate required by the XD for the same $n_{e,sep}$ will be discussed in section 4.3.4.

4.2 Advantages of XD on detachment

In this section I compare the SD and XD performance on SOL detachment and discuss how the differences are attributed to the geometric characteristics.

Let me begin by inspecting the density threshold for detachment using a gas-puff-rate scan. The relationships between the peak target electron temperature and

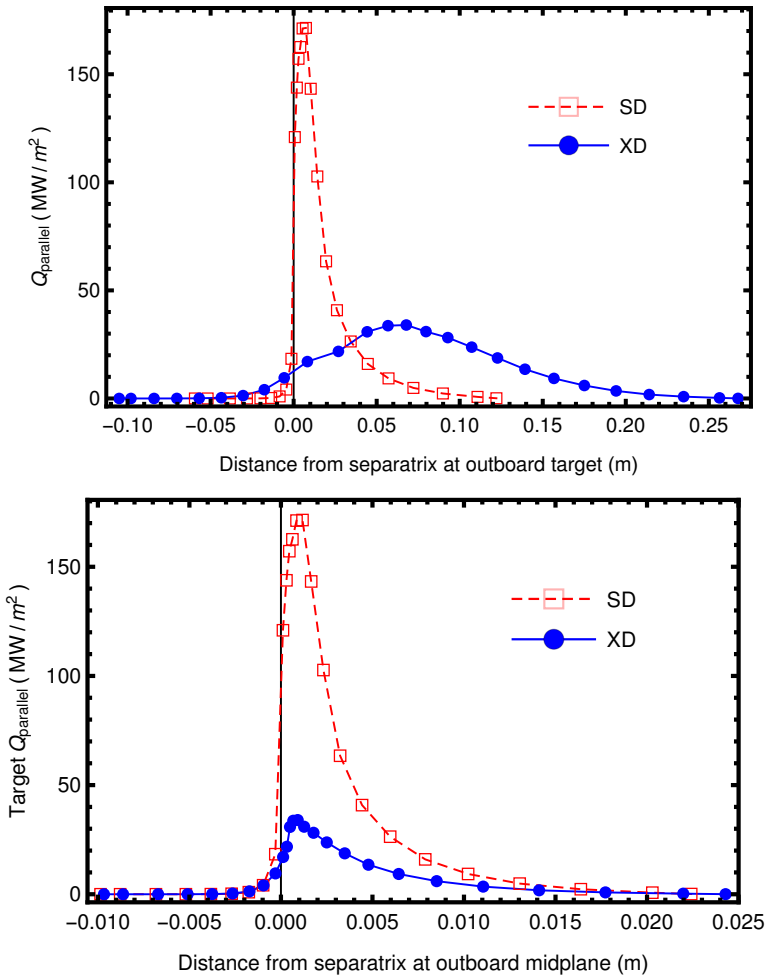

Figure 4.5: The radial profiles of $Q_{\|}$ at outboard target for the SD and XD cases.

the electron density at upstream (outboard midplane) separatrix, $n_{e,sep}$, are shown in Fig. 4.8. Let the *detachment onset* be defined as the condition where the peak target temperature is about 5eV and target to upstream pressure ratio is about 50%. The XD geometry has a density threshold $n_{e,sep} \sim 2.85 \times 10^{19}\mathrm{m}^{-3}$ for detachment onset onset compared to $n_{e,sep} \sim 3.56 \times 10^{19}\mathrm{m}^{-3}$ for the SD. In terms of the gas puff rate, the XD begins detachment at $\sim 6.2 \times 10^{21}$ particles/s while for the SD, the corresponding rate is $\sim 7.8 \times 10^{21}$ particles/s; the XD achieves a similar level of detachment at about 25% lower density. This is similar to results found for DIII-D simulations and experimental results [9].

Poloidal flaring is the principal geometric characteristic behind the benefits ac-

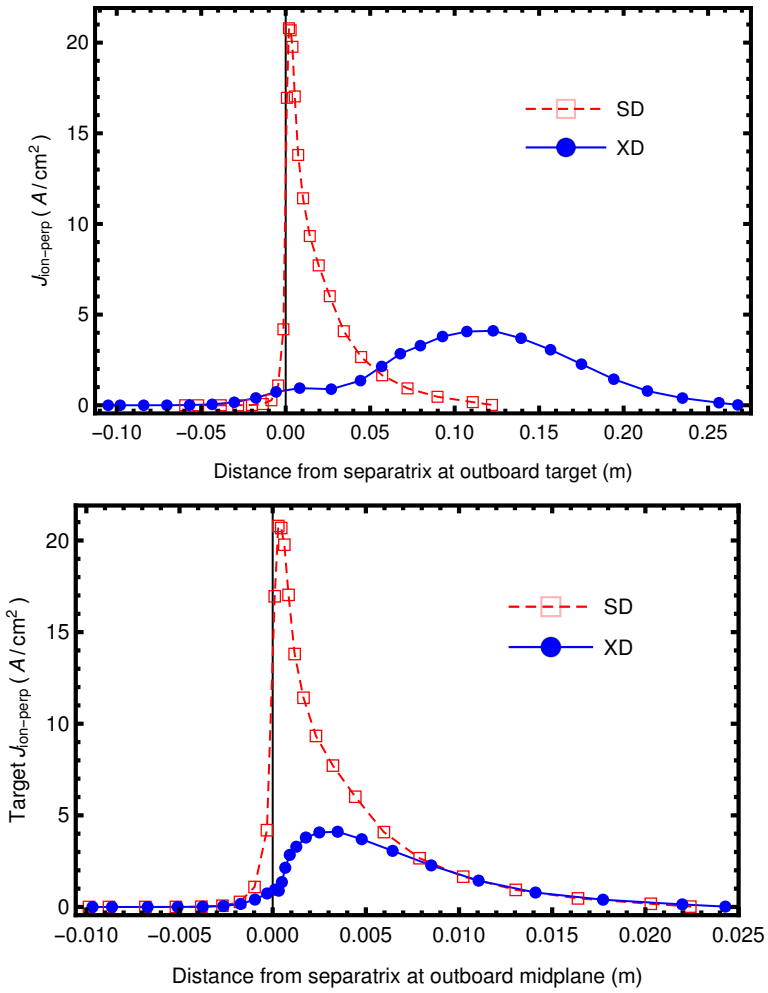

Figure 4.6: The radial profiles of $J_{ion,\perp}$ at outboard target for the SD and XD cases. J_{ion} is the ion contribution to the total electric current, which is the synonym of ion flow.

crued through XD. As the SOL plasma approaches detachment, a neutral gas buffer layer is developed near the target. As discussed in section 2.2.3 strong plasma-neutral interaction takes place within the buffer layer. The fact that the XD distributes a substantial amount of connection length within the neutral buffer (Fig. 3.5) and hence has a much larger interaction length is crucial. So the plasma particles have a higher chance to lose their energy/momentum before hitting the target in the XD configuration than in the SD. In other words, the neutral buffer is used much more efficiently by the XD. Therefore the peak target T_e is lower for the XD (Fig. 4.8) at similar upstream density $n_{e,sep}$. By contrast, the interaction length of the SD shrinks

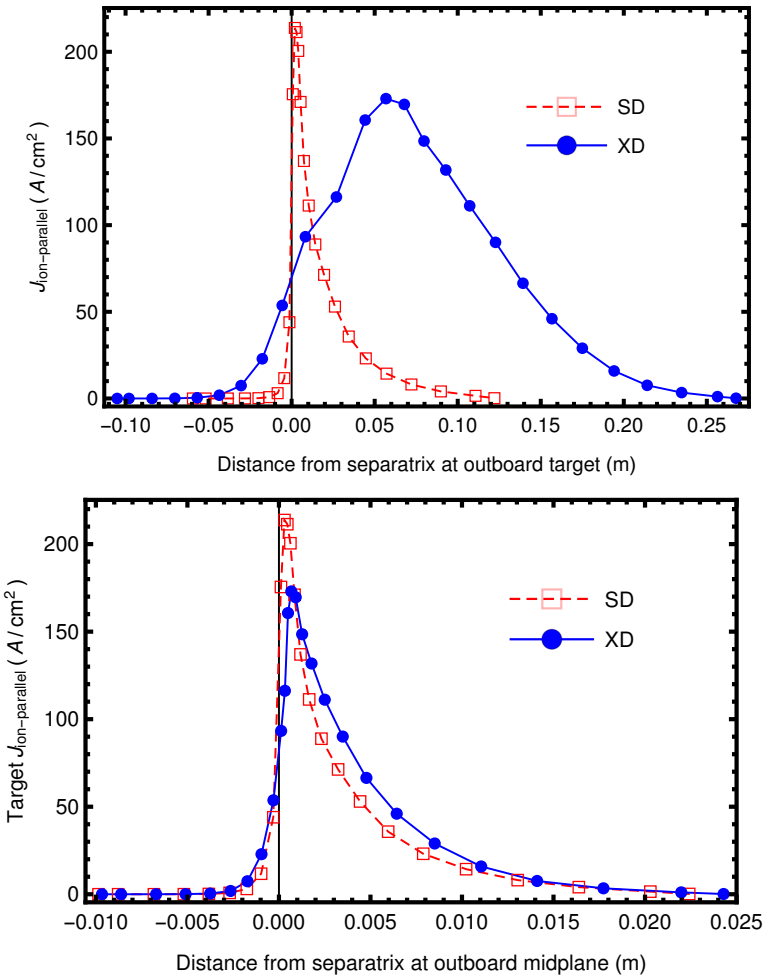

Figure 4.7: The radial profiles of $J_{ion,\parallel}$ at outboard target for the SD and XD cases.

as it enters the neutral buffer, so it needs a thicker neutral gas buffer to make the plasma detached, namely the SD needs a higher neutral gas-puff rate.

In the previous section the two divertors are compared at similar upstream density $n_{e,sep} \sim 3.3 \times 10^{19}\mathrm{m}^{-3}$; we find the XD to be detached while the SD is not. It is also important to compare the divertors when both are detached (with similar downstream conditions).

Now, I will examine the "stability" of the detachment front for the two divertor configurations. For this purpose I compare the SD and the XD cases at two states of detachment: 1) at the onset of detachment (defined above), and 2) when both reach a full detachment. The latter is defined as the state when the peak target T_e drops to ∼2 eV. (At full detachment, $n_{e,sep} \sim 3.89 \times 10^{19}\mathrm{m}^{-3}$ for the SD and

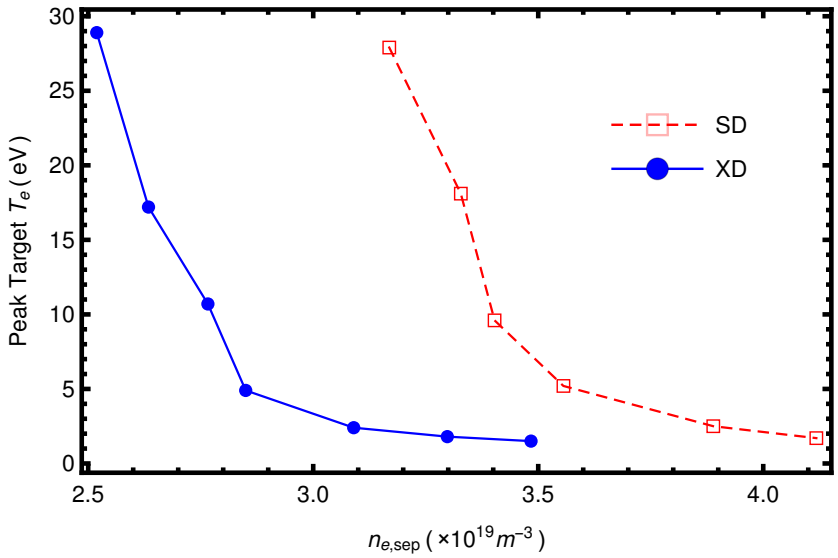

Figure 4.8: The relation between the peak target electron temperature and the separatrix electron density at upstream (outboard midplane) for the SD and XD geometries.

$n_{e,sep} \sim 3.08 \times 10^{19}\mathrm{m}^{-3}$ for the XD.)

Shown in Figs. 4.9 and 4.10 are the poloidal profiles of the total plasma pressure (p_{tot}), and the parallel heat flux ($Q_{\|}$) for the two divertors. Clearly the XD does a better job than the SD in stabilizing the detachment front: the front (indicated by the steep gradient of p_{tot} and $Q_{\|}$) is closer to the target for the XD. Furthermore as the SOL plasma enters a deeper state of detachment the front in the SD configuration migrates upstream toward the core X-point whereas the detachment front in the XD configuration is localized in the region near the divertor plate.

Let me now try to explain how the divertor magnetic structure directly affects the formation and stability of the detachment front. As mentioned in section 2.2.3, the plasma energy and momentum losses in the divertor region are closely related to the interaction length, $\triangle l$: the longer $\triangle l$ is in a given increment of poloidal distance (or perpendicular neutral mean free path) the higher the energy and momentum losses within that poloidal section. For SD, $\triangle l$ in a unit increment of poloidal distance increases monotonically upwards towards the main X-point (the angle θ decreases monotonically (Fig. 3.4 and Fig. 3.5)). Consequently, the energy and momentum losses increase. This positive feedback of the SD tends to cause a radiation collapse

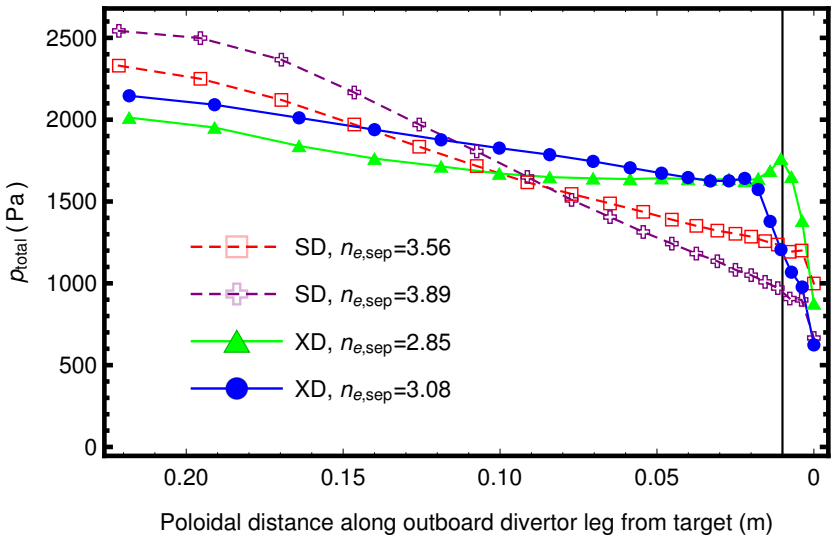

Figure 4.9: The poloidal p_{tot} profiles for the SD and the XD configurations both at detachment onset and full detachment. The vertical line indicates the location of the detachment front in the XD cases. The flux surfaces for these 1D profiles were chosen based on the location of the peak values at the divertor entrance. The upstream densities $n_{e,sep}$ have the unit of $10^{19}m^{-3}$.

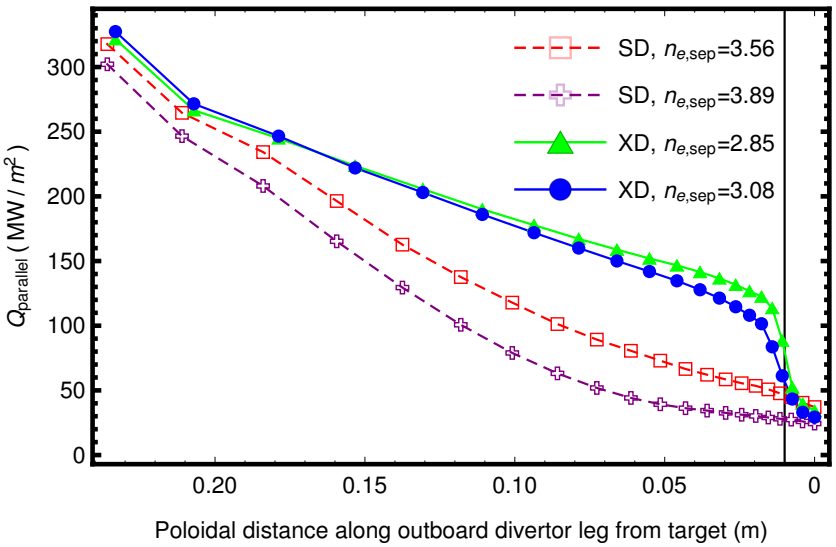

Figure 4.10: The poloidal $Q_{\parallel}$ profiles for the SD and the XD configurations. The vertical line indicates the location of the detachment front in the XD cases. The flux surfaces for these 1D profiles were chosen based on the location of the peak values at the divertor entrance. The upstream densities $n_{e,sep}$ have the unit of $10^{19}m^{-3}$.

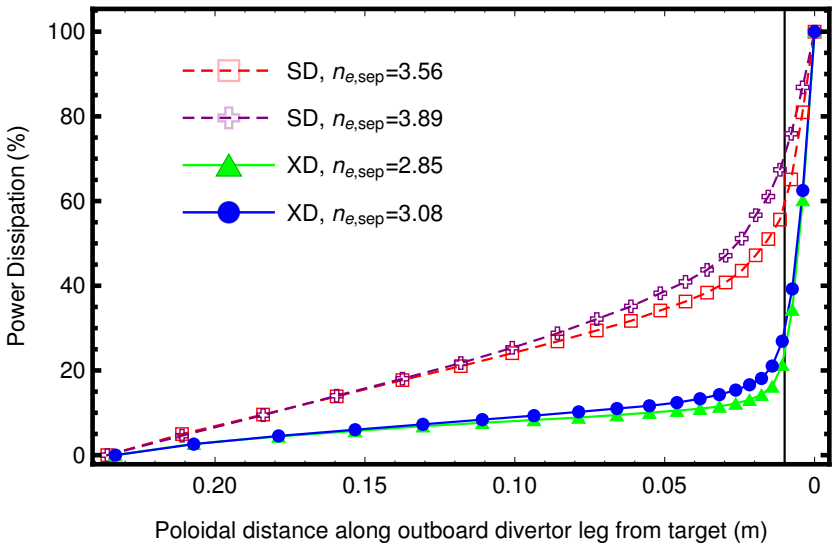

Figure 4.11: The poloidal power dissipation profiles for the SD and the XD configurations. Each value is the ratio of the power dissipated between the divertor entrance and that poloidal location to the total power dissipated in the whole divertor region. The vertical line indicates the location of the detachment front in the XD cases. The upstream densities $n_{e,sep}$ have the unit of $10^{19}m^{-3}$.

of the detachment front so that it tends to move further upwards towards the heat source —the main plasma. By contrast the XD has a stabilizing feedback in the region of poloidal flaring: since the angle θ increases, $\triangle l$ in a unit increment of poloidal distance decreases as it goes upwards away from the target; the energy and momentum loss mechanisms are weakened, and so upstream migration of the detachment front is resisted/discouraged. Such explanation is consistent with the simulation results shown in Fig. 4.11: for the SD, a substantial portion ($\sim$ 60%) of the power is dissipated in the upstream divertor region, whereas for the XD, most of the power dissipation ($\sim$ 75%) happens within the neutral buffer layer close to the target. For more detailed explanations see Ref. [20].

A thought experiment will clarify these ideas further. Suppose that one were to tilt the SD plate to make the wetted area and connection length equal the corresponding XD values. One may, then, expect that the two geometries will reach detachment onset at similar $n_{e,sep}$ or gas-puff rates. However, due to the differences in their geometric characteristics, one finds that the SD with a tilted plate facilitates the

front to migrate upward (towards the main X-point) whereas the XD resists it. It must be noted that the stabilizing effect is unique to the XD poloidal flaring; it can not be achieved by simply tilting the divertor plate of an SD even if the required significant hardware changes were made.

To wrap up this section, I will now compare the two SOL properties that are crucial to tokamak power exhaust; the SD and the XD will be compared at similar states of detachment.

First I consider the upstream SOL by comparing the electron temperature (T_e) profiles. With the benefits of a longer connection length and detaching at a lower $n_{e,sep}$, the XD cases exhibit a $\sim 30\%$ higher upstream T_e. Furthermore since the XD stabilizes the front close to the target as demonstrated above, its T_e profile has a steeper gradient at the front compared to the SD (Fig. 4.12). As mentioned in the introduction, one of the goals of XD invention/development is to achieve detachment without degrading the core plasma. The results have confirmed the success of XD: the hot core plasma upstream is better insulated from the cold plasma and neutral gas downstream. Hence the good H-mode energy confinement is preserved by the XD.

Last I consider the downstream SOL by comparing the perpendicular heat flux ($Q_\perp$) profiles. Not only is the heat more spread across the divertor plate by the XD but the peak $Q_\perp$ is also reduced by a factor of $3 \sim 4$ (Fig. 4.13). Thus during tokamak operation the exhaust power flux can be handled more effectively with the XD. The XD can increase target lifetime by largely reducing $Q_\perp$ and reducing the plate temperature and hence plate erosion due to sputtering.

4.3 Some remarks

4.3.1 On SOL width

Following the experimentalists' standard way to determine the SOL width, one plots the $Q_\perp$ profile at the target (like the ones shown in Fig. 4.13) as a function of the position of each flux surface at outboard midplane upstream [Fig. 4.14 (similar to Fig. 2.4)] and simply reads off the e-folding length. The simulated SOL width is $\sim$ 3mm,

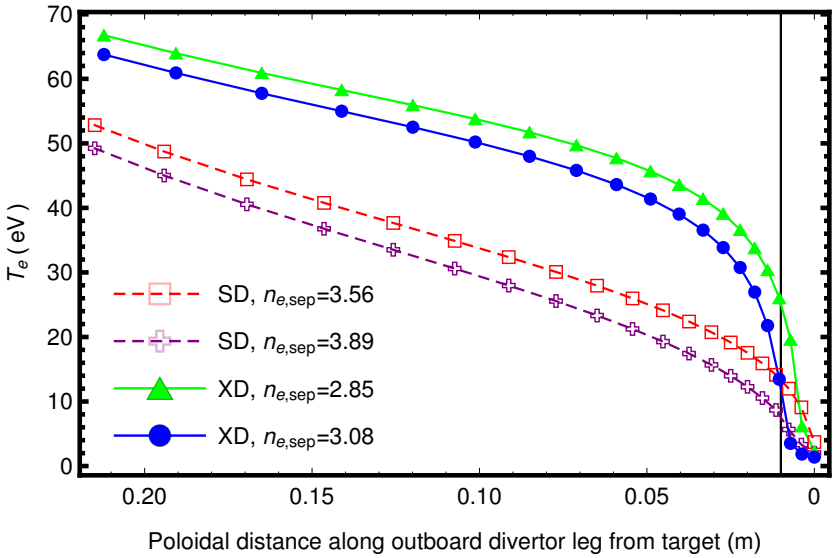

Figure 4.12: The poloidal temperature profiles for the SD and XD cases. The vertical line indicates the location of the detachment front in the XD cases. The flux surfaces for these 1D profiles were chosen based on the location of the peak values at the divertor entrance. The upstream densities $n_{e,sep}$ have the unit of $10^{19}m^{-3}$.

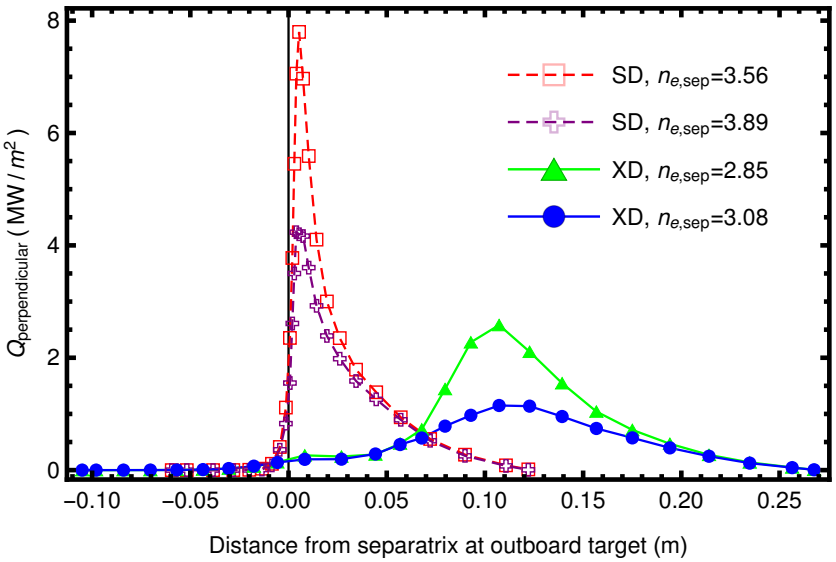

Figure 4.13: The radial profiles of $Q_\perp$ at outboard target for the SD and XD cases both at detachment onset and full detachment. The upstream densities $n_{e,sep}$ have the unit of $10^{19}m^{-3}$.

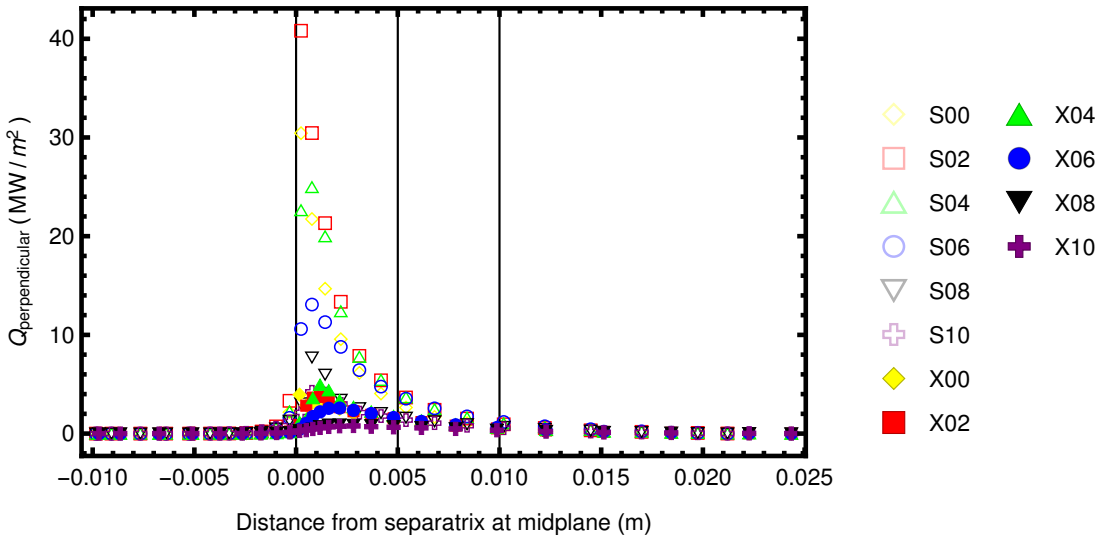

Figure 4.14: SOL width determined by mapping the target $Q_\perp$ profile to upstream positions. The value is consistent for all gas-puff rates.

which is within the range of experimental results. Thus the choice of perpendicular transport coefficients is reasonable.

4.3.2 On T_e profile and simple model

By the simple SOL model in section 2.1, T_e along a field line varies, to the lowest order, as $l^{2/7}$ (Eq. 2.3). However, this relationship breaks down as higher order corrections due to energy dissipation are added. To check how far off the lowest order prediction from the more accurate result from the full model is, I compare the two by plotting T_e profiles along a field line in Fig. 4.15. The theoretical estimate is based on Eq. 2.3 using the upstream $Q_\parallel$ and target T_e from simulation.

By comparison, it can be seen that the deviation from the lowest order model is bigger for the XD than for the SD, especially in the downstream region near the target. This is consistent with the fact that the XD has a larger interaction length downstream near the target and has higher level of plasma-neutral interactions which cause the deviation.

Because of this, when the T_e profiles are plotted along the field lines, the XD cases look different from the SD cases (Fig. 4.16). It is the plasma-neutral interactions

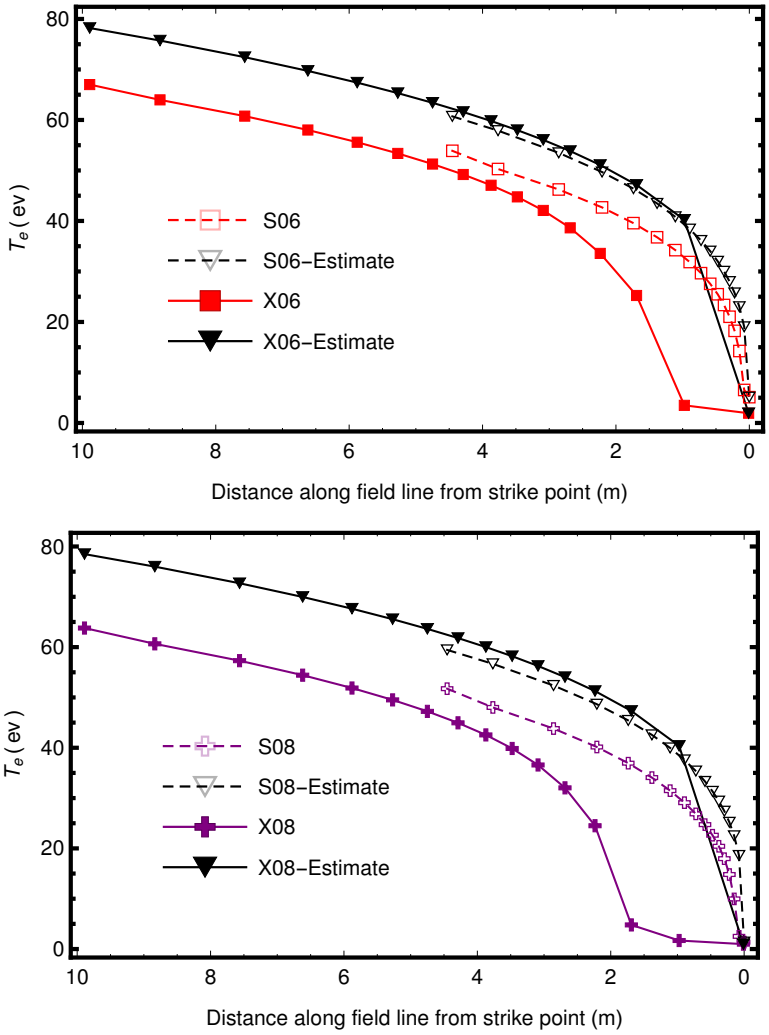

Figure 4.15: T_e profiles along a field line by simulation and simple model estimation. The cases with gas-puff rates $6 \times 10^{21}\mathrm{s}^{-1}$ (top) and $8 \times 10^{21}\mathrm{s}^{-1}$ (bottom) are shown.

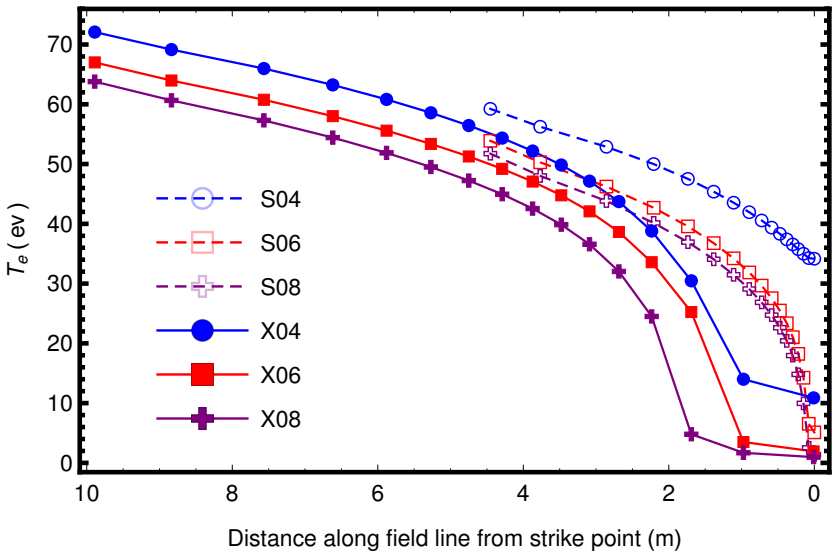

Figure 4.16: T_e profiles along field lines. The SD and the XD cases are compared at the same gas-puff rates.

that really distinguish the different divertor geometries; it is not simply the total connection length, but also the distribution of connection length that matters.

4.3.3 On recycling in the private region

The private region is separate from the divertor SOL by the separatrix. The recycling in the private region provides abundant neutrals that have been found to be important to SOL plasma cooling. It is generally took for granted that the parallel heat flux $Q_{\parallel}$ remains constant for the most part along the field line until it reaches the neutral buffer very close to the target. This is true for the flux surfaces some distance away from the private region. For example along the field line on a flux surface that is 0.6mm away from the separatrix at midplane, $Q_{\parallel}$, indeed, mostly remains constant (the bottom graph in Fig. 4.17). However since the neutrals in the private region penetrate into the SOL which causes substantial plasma-neutral interaction, $Q_{\parallel}$ decreases along a field line on a flux surface that is 0.3mm away from the separatrix at midplane (the top graph in Fig. 4.17). This is a very important to SOL cooling since the exhaust heat concentrates within the narrow SOL width close to the separatrix.

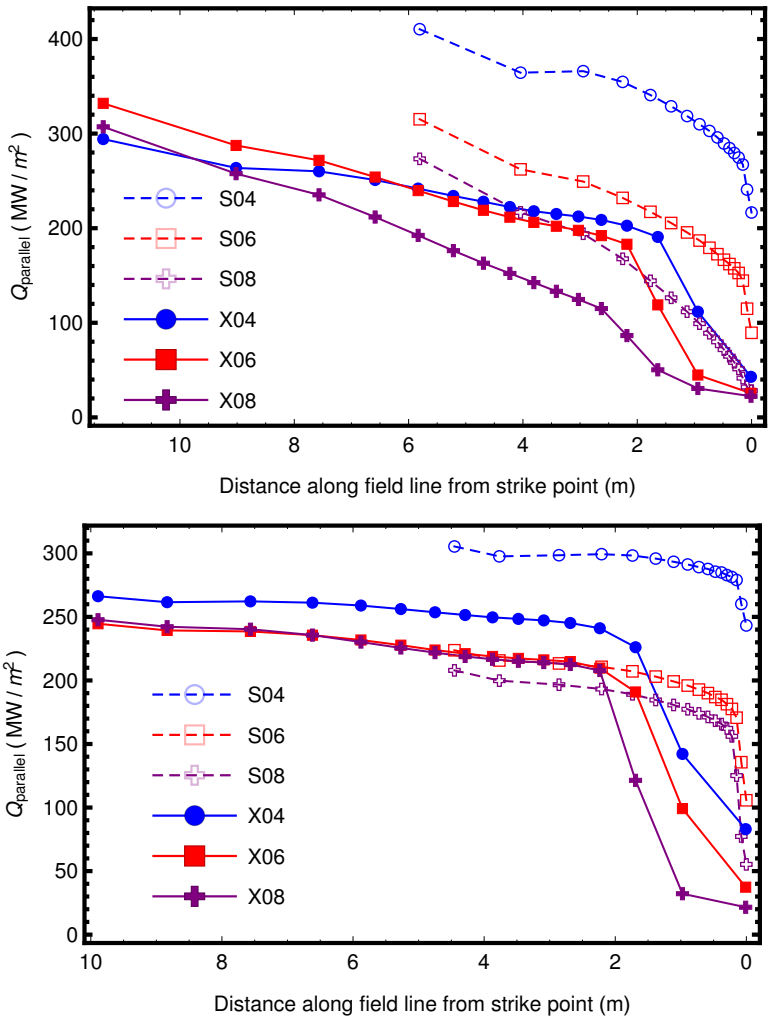

Figure 4.17: $Q_{\parallel}$ profiles along a field line on flux surfaces that are 0.3mm (top) and 0.6mm (bottom) from the separatrix at midplane.

4.3.4 On the dependence of $n_{e,sep}$ on gas-puff rate

It is found that for the same gas-puff rate, the plasma density upstream at the separatrix, $n_{e,sep}$, is consistently lower in XD than in SD (see Tab.4.1).

A possible explanation is as follows. A steady state is reached when the pumping rate balances the puffing rate. Previous heuristic arguments, and SOLPS simulations, indicate that when the SD and XD configurations have similar values of upstream $n_{e,sep}$, the XD case has a higher degree of detachment. Greater detachment is expected to have, associated with it, a higher neutral density and a higher neutral pressure near

gas rate ($10^{21}/s$)	$n_{e,sep}$ ($10^{19}m^{-3}$), SD	$n_{e,sep}$ ($10^{19}m^{-3}$), XD
2	2.007	1.828
4	2.616	2.353
6	3.198	2.789
8	3.641	3.120
10	3.880	3.377

Table 4.1: The dependence of $n_{e,sep}$ on gas-puff rate

the target. For a given upstream $n_{e,sep}$, a higher neutral pressure near the target will cause a higher pumping rate for the XD configuration. Hence, a higher puff rate will be needed to attain that value of upstream $n_{e,sep}$. Or equivalently, when the puff rate is the same for both configurations, the XD case has a lower upstream $n_{e,sep}$.

4.3.5 On validating the physics in experiments

Ultimately, the advantages of advanced divertors have to be demonstrated experimentally before they can be considered for future fusion devices. A few divertor experiments have been done on tokamaks: TCV,[22] NSTX,[27] DIII-D [9, 7] and MAST. It is important to know the capabilities of experimental techniques in order to plan experiments.

First, to show that XD can make it easier for the SOL to detach, IR thermography is needed to monitor the target temperature and heat flux as the upstream density varies. The saturation current can also be measured using probes and be related to the ion flux. Then, to show that XD is better than SD in stabilizing the detachment front, one can use bolometry (if the resolution in the divertor region is well enough) to map the radiated power structure and compare that with the radiation pattern simulated by SOLPS. If there is a carbon light for the divertor region, that is also a great way to visualize the behavior of detachment front. Fig. 4.18 shows an example of radiation and carbon emission pattern in the most recent DIII-D experiment [9].

A different view point can also be taken when doing analysis. That is to pick shots of XD and SD cases that have the similar downstream conditions and look at

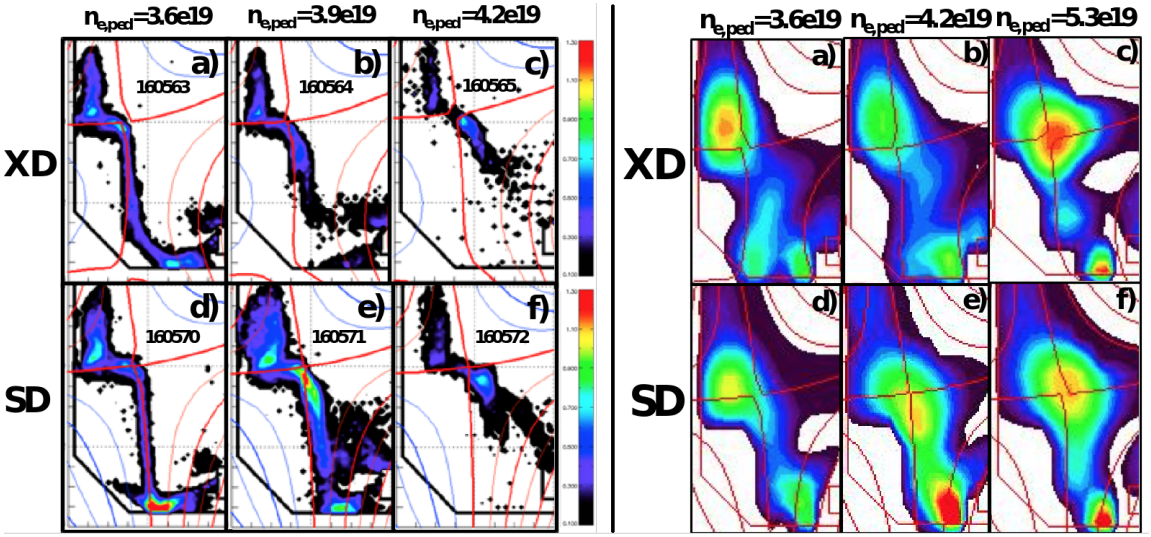

Figure 4.18: The C^{3+} emission pattern (left) and radiation pattern (right) showing that the XD facilitates detachment with lower upstream density and stabilizes the detachment front keeping the highly radiating region close to the target.

the upstream properties. For example when the SD and the XD have similar target temperature and peak heat flux, one can compare density and pressure at pedestal top and midplane temperature profile measured by Thompson scattering. The physics to be demonstrated is when the SD and XD have similar state of SOL detachment the XD has a better H-mode, a better core energy confinement. It has been shown in section 4.2 using SOLPS simulations that when the downstream conditions are similar, the XD case has a lower $n_{e,sep}$ and also a higher $T_{e,sep}$. It is believed that a lower $n_{e,sep}$ and a higher $T_{e,sep}$ indicate a better H-mode quality. However, the n_{ped} and p_{ped} in the pedestal are beyond SOLPS' capability. So this can only be proved by experiments.

Appendix A

Concepts for Magnetic Confinement Fusion

A.1 Nuclear Fusion: A Promising Energy Source

When lighter atomic nuclei fuse to form heavier nuclei (generally with the emission of neutrons and/or protons), very large amount of energy (per reacting nucleon) is released. The fusion of hydrogen nuclei into helium, for example, is the main reaction that powers the stellar interiors. Since the 1950s, there has been an ambitious effort to create "suns" on the earth. That is, to build power plants that use nuclear fusion as an energy source.

Fusion energy has advantages over other energy sources. First it is a relatively clean energy source. Unlike chemical processes like combustion used to produce energy from fossil fuel, nuclear reaction has no air-polluting by-products.The problem of radioactive by products, though a serious problem for nuclear fission, is expected to be rather solvable for fusion.

Second it is very reliable. Fusion technology is not subject to local external conditions. Therefore it can guarantee base load power production which other ecologically friendly sources like wind and solar energy can not guarantee. Finally, it is sustainable. Clean fusion energy can support human society for thousands if not tens of thousands of years since the fueling hydrogen isotope deuterium in ordinary seawater is abundant. It is estimated that nearly three-quarters by mass of the known matter in the universe is hydrogen which gives fusion energy a bright future in view of future human exploration into space.

The success of controlled fusion does offer a long term if not the ultimate solution to the power consumption problem of human society. That is, perhaps, why fusion is still on the scientific agenda despite the fact that success in controlled fusion has

eluded us for more than 60 years of trying.

A.2 Fusion Technology, the Triple Product

If a single number could index the progress towards fusion energy, then the so called triple product,

$$Triple\,product = nT\tau \tag{A.1}$$

, (where n, T , and τ, are respectively the density, the temperature and the confinement time of the plasma) is our best guide.

The triple product, rightly, is the basis for characterizing all thermonuclear fusion technologies, no matter how different their mechanisms of operation. Some methods rely on pushing the fusion fuel to extreme densities only for a few nanoseconds, while other methods aim to confine the fuel at sparse density for large times. Either way, the desirable conditions for fusion reactions are: hotter, denser, longer.

The sun (or stars) is an example of natural energy producing fusion reactor. It has a very high density (on the order of 10^{32}particles$/m^3$) and a sufficiently high temperature (on the order of 10^7K), gravitationally confined (permanently) plasma so that steady-state fusion is possible.

Unfortunately the condition for fusion prevalent in the sun- the high density and gravitational confinement- are not achievable on earth. We need to look for some other ways.

One thing we can do is making the choice of fusion fuel. Hydrogen fusion has the highest energy gain per nucleon so it is natural to explore the three isotopes of hydrogen – protium (H-1), deuterium (D, H-2), and tritium (T, H-3). It is found that D-T fusion reaction is the most favorable candidate for fusion technology. The reason is that the cross section for D-T collision is the highest (much higher than the cross section for H-H collision in the sun) for a temperature range that is hopefully achievable in a fusion reactor.

The biggest challenge today is plasma confinement.

A.3 Magnetic Confinement and the Tokamak

For the purpose of this research we focus on magnetic confinement fusion (MCF).

The MCF method falls into the low-density (to date $\sim 10^{20}$ particles/m^3), high-confinement time (to date $\sim$ 1s) region of the triple product spectrum. Because of the relatively low density, which makes confinement relatively easier, the confinement time has to be substantially increased to reach a triple product high enough for fusion energy purposes.

Unlike the sun which uses its natural gravity to confine the plasma, MCF uses strong, closed magnetic fields to tightly confine a plasma. The constituent parts of a plasma – electrons and ions – gyrates along magnetic field lines due to Lorentz force. In this way the motion of the charged particles perpendicular to the magnetic field is confined. Yet, they are still free to move along the magnetic field lines. A simple idea is to let the magnetic field line close on its own (or equivalently form a closed surface in 3D space) such that the charged particles move in an infinite loop, and thus be confined. This is the underlying idea behind tokamaks and stellarators. This research is related to tokamak only.

The tokamak, due to the relative simplicity of its design, is the MCF devices of choice and has already demonstrated steady and impressive experimental progress. Tokamak has a hollow, axisymmetric torus-like vacuum vessel, inside which the plasma is confined. A set of looped coils are linked to the torus. They create a toroidal magnetic field to confine the plasma and are called toroidal field (TF) coils (Fig. A.1).

For the purposes of heating and improved confinement, a toroidal plasma current is also induced, which generates its own poloidal magnetic field. The superposition of the toroidal and poloidal magnetic fields results in helical field lines inside the torus (Fig. A.2). In addition, there are also loop coils that carry currents in the toroidal direction producing extra poloidal magnetic field. They are called the poloidal field (PF) coils. The PF coils play a major role in controlling the shape and location of the plasma and they are crucial to this research.

The radius from the axis of symmetry to the plasma center is known as the plasma major radius, R_0, while the radius of the plasma cross-section in the poloidal plane is the minor radius, a. The aspect ratio of a tokamak is simply the ratio between these two radii, R_0/a. There are high aspect ratio ($2 \sim 3$) machines and low aspect ratio ones (~ 1). For example ITER is a high aspect ratio tokamak where as NSTX-U is

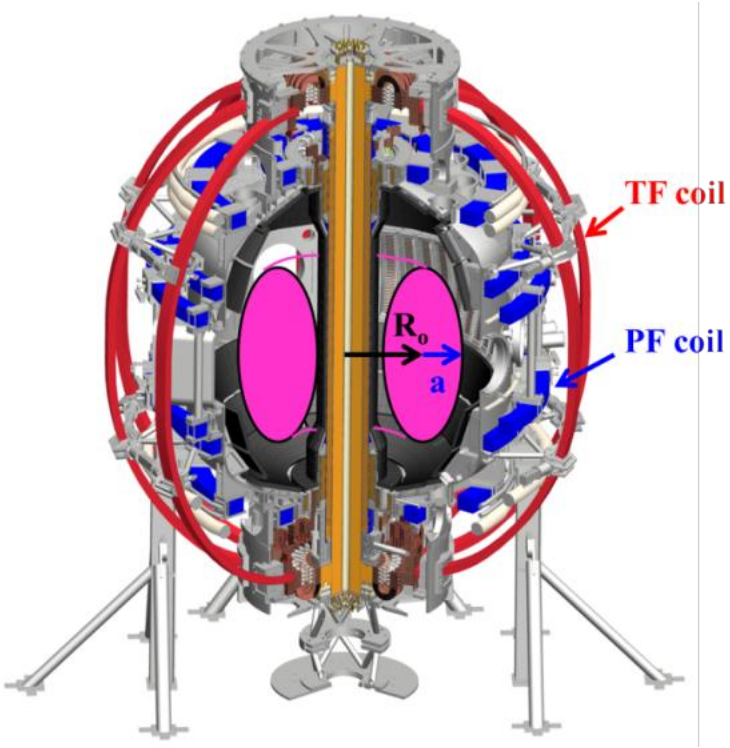

Figure A.1: A cutaway of the NSTX tokamak[5]. TF coils and PF coils are marked in red and blue respectively. The major radius (R_0) and the minor radius a are indicated.

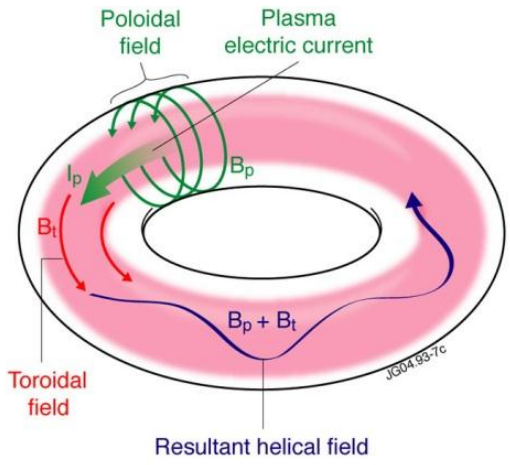

Figure A.2: The helical magnetic field as a combination of the TF field and the PF field. Plasma is better confined using helical magnetic field instead of TF field alone. Figure courtesy of the EFDA [6].

a low aspect ratio tokamak. Tokamaks with aspect ratio approaching 1 are generally referred to as spherical tokamaks.

The confinement provided by the helical magnetic field is not perfect. There is plasma leaking out from the "magnetic bottle" and reaching the wall of the vacuum vessel. As the fusion triple product is pushed further, this issue becomes serious. This research is about the physics regarding the interaction between the hot plasma and the cold solid wall material —scrape-off-layer and divertor physics.

Appendix B

CORSICA for Magnetic Equilibrium

The CORSICA code is capable of calculating magnetic equilibria. It calculates free boundary equilibria by solving the Grad-Shafranov equation and doing minimisation iteratively. The method is outlined in this section.

B.1 Solving the Grad-Shafranov Equation

To describe the magnetic field in a tokamak, a cylindrical coordinate system $\{R,\, \varphi,\, z\}$ is used where R is the radial distance from axis of symmetry, z is the coordinate along the axis, and φ is the toroidal angle.

The magnetic field in an axisymmetric system, like a tokamak, can generally be written as

$$\boldsymbol{B} = \nabla\varphi \times \nabla\psi + F\nabla\varphi \tag{B.1}$$

where ψ is the stream function for the poloidal component of the magnetic field vector, and $F = RB_t$ with $B_t = \boldsymbol{B} \cdot \mathbf{e}_\varphi$.

For axisymmetric configurations with no flow, the equilibrium ψ satisfies the Grad-Shafranov equation [14] :

$$\triangle^*\psi = -\frac{1}{\mu_0}R^2\frac{\partial p}{\partial \psi} - F\frac{\partial F}{\partial \psi} \tag{B.2}$$

where the elliptic operator $\triangle^*$ is defined by

$$\triangle^*\psi \equiv R^2\nabla \cdot \frac{1}{R^2}\nabla\psi \tag{B.3}$$

In order to solve equation B.2, the functions $p\,(\psi)$ and $F\,(\psi)$ must be specified. In practice, usually the pressure profile $p\,(\psi)$ and the profile of the flux surface average of $\boldsymbol{j}\cdot\boldsymbol{B}/B^2$ are specified, where $\boldsymbol{j}$ is the current density. F has a nonlinear relationship with p and $\langle \boldsymbol{j}\cdot\boldsymbol{B}\rangle \,/\, \langle B^2\rangle$; and can be numerically calculated.

Once $p(\psi)$ and $F(\psi)$ are known, the last piece needed to solve equation B.2 is a boundary condition. In the case of CORSICA code, the boundary condition is set in the following manner: specifying the shape of the separatrix and requiring that ψ being constant along the separatrix as well as $\boldsymbol{B}_p \equiv \nabla\varphi \times \nabla\psi = 0$ at the X-point.

Once $\psi(R, \varphi, z)$ is obtained, the information of the magnetic field can be calculated numerically and the flux surfaces can be plotted as contours of ψ.

B.2 Calculating Free Boundary Equilibria

Once the stream function ψ is solved from the Grad-Shafranov equation, the total magnetic field can be calculated and then the current can be calculated based on the magnetic field, both inside and outside the separatrix. The current outside the separatrix is non-zero in general. That means in order to obtain a ψ that satisfies the desired separatrix shape, not only the plasma current inside the separatrix but also external current outside the separatrix is necessary. The current outside the separatrix is a continuous current density distribution which has an infinite degree of freedom. Nevertheless, in reality the external current is provided by a set of PF coils which has a finite degree of freedom. Therefore in reality one can never get a separatrix that is exactly the same as desired. In order to make an equilibrium achievable in experiments, one must perform a *free boundary* calculation to obtain the equilibrium.

In CORSICA code, the free boundary calculation is done in the following manner.

First, the user specifies a desired separatrix shape by specifying a number of boundary points. There are two types of boundary points: fixed points and fuzzy points (Fig. B.1). Fixed points have infinite weights such that the calculated separatrix must go through them. The fuzzy points have finite weights that can be adjusted individually for each point by the user.

Second, the user specifies a set of PF coils with their locations, sizes and the desired currents. Each PF coil is also associated with a weight controlling how much the code can adjust the current from the desired value. A coil whose current must be fixed has an infinite weight.

During the calculation, the code first makes a guess for a separatrix shape and a set of coil currents. The guess is made with the attempt to minimize the deviation

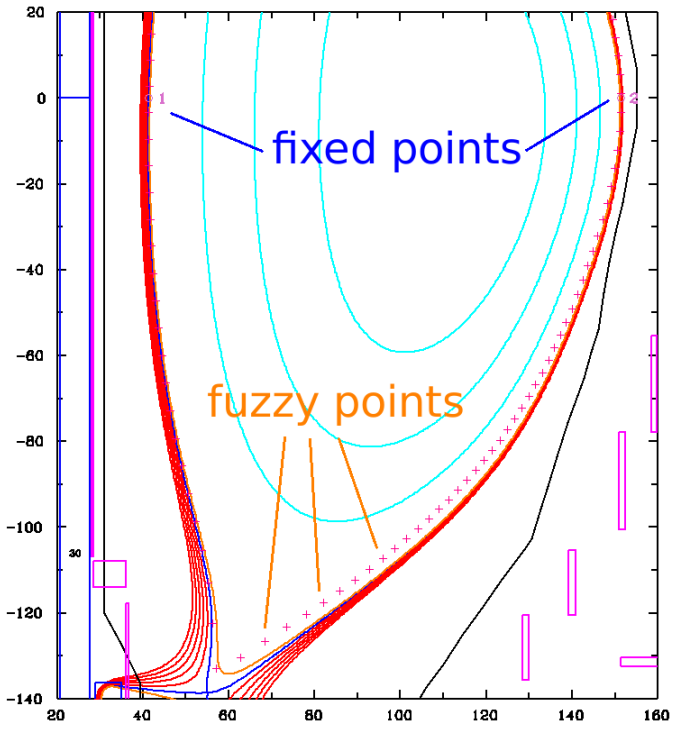

Figure B.1: Fixed and fuzzy points used in CORSICA.

between the guessed separatrix and the desired shape and also to minimize the deviation of the currents from the desired values. Then it solves the Grad-Shafranov equation with the guessed separatrix as the boundary condition. Once the ψ is obtained, it calculates the actual external current distribution based on the ψ. The difference between the actual external current distribution and the guessed coil currents is evaluated. Based on the difference, the code makes a new guess changing both the separatrix shape and the coil currents and starts the next iteration. The iteration stops when either the user specified residual to the Grad-Shafranov equation is reached or the maximum number of iterations is reached.

Appendix C

SOLPS for Transport Modeling

SOLPS code is a package of several codes working together for SOL physics study.

The two most important codes are the B2.5 code for plasma physics modeling and the Eirene code for neutral physics modeling. Basic explanations with some technical details for these two codes are covered in the following sections.

The other codes in the package are used to prepare the set of input files for B2.5 and Eirene. They will not be discussed here.

C.1 B2.5 for SOL Plasma Modeling

In the fluid approach the SOL plasma is described by Braginskii equations [8] which are summarized below.

The continuity equation for ions:

$$\frac{\partial n_i}{\partial t} + \nabla \cdot (n_i \boldsymbol{v}_i) = S_{n_i} \tag{C.1}$$

and electrons:

$$\frac{\partial n_e}{\partial t} + \nabla \cdot (n_e \boldsymbol{v}_e) = S_{n_e} \tag{C.2}$$

The momentum equations for ions:

$$\frac{\partial}{\partial t}(m_i n_i \boldsymbol{v}_i) + \nabla \cdot (m_i n_i \boldsymbol{v}_i \boldsymbol{v}_i) = -\nabla p_i - \nabla \overleftrightarrow{\Pi}_i + Z_i e n_i (\boldsymbol{E} + \boldsymbol{v}_i \times \boldsymbol{B}) + \boldsymbol{R}_i + \boldsymbol{S}_{\boldsymbol{v}_i} \tag{C.3}$$

and electrons (neglecting inertia, often called the generalized Ohm's law):

$$-\nabla p_e - e n_e (\boldsymbol{E} + \boldsymbol{v}_e \times \boldsymbol{B}) + \boldsymbol{R}_e = 0 \tag{C.4}$$

with

$$\boldsymbol{R}_e = -\boldsymbol{R}_i = e n_e \left(\frac{\boldsymbol{j}_\parallel}{\sigma_\parallel} + \frac{\boldsymbol{j}_\perp}{\sigma_\perp} \right) - 0.71 n_e \nabla_\parallel T_e - \frac{3}{2} \frac{e n_e^2}{\sigma_\perp B^2} \boldsymbol{B} \times \nabla T_e \tag{C.5}$$

including loss due to Ohmic heating, loss due to friction of electrons with different temperature parallel to B and thus different thermal velocities and loss due to deflection of electrons at temperature gradients perpendicular to B. The total electric current is defined as:

$$\boldsymbol{j} = e\left(Z_i n_i \boldsymbol{v}_i - n_e \boldsymbol{v}_e\right) \tag{C.6}$$

The total energy equations for ions:

$$\frac{\partial}{\partial t}\left(\frac{3}{2}n_i T_i + \frac{m_i n_i}{2}v_i^2\right) + \nabla\cdot\left[\left(\frac{5}{2}n_i T_i + \frac{m_i n_i}{2}v_i^2\right)\boldsymbol{v}_i + \overleftrightarrow{\Pi}_i \cdot \boldsymbol{v}_i + \boldsymbol{q}_i\right] = \left(Z_i e n_i \boldsymbol{E} - \boldsymbol{R}\right)\cdot\boldsymbol{v}_i - Q_{ei} + S_{E_i} \tag{C.7}$$

and electrons (simplified):

$$\frac{\partial}{\partial t}\left(\frac{3}{2}n_e T_e\right) + \nabla\cdot\left(\frac{5}{2}n_e T_e \boldsymbol{v}_e + \boldsymbol{q}_e\right) = -e n_e \boldsymbol{E}\boldsymbol{v}_e + \boldsymbol{R}\cdot\boldsymbol{v}_i + Q_{ei} + S_{E_e} \tag{C.8}$$

The set of equations is closed by the energy fluxes for ions:

$$\boldsymbol{q}_i = -\kappa_\parallel^i \nabla_\parallel T_i - \kappa_\perp^i \nabla_\perp T_i + \kappa_\wedge^i \frac{\boldsymbol{B}}{B}\times\nabla_\perp T_i \tag{C.9}$$

and electrons:

$$\boldsymbol{q}_e = -\kappa_\parallel^e \nabla_\parallel T_e - \kappa_\perp^e \nabla_\perp T_e + \kappa_\wedge^e \frac{\boldsymbol{B}}{B}\times\nabla_\perp T_e - 0.71\frac{T_e}{e}\boldsymbol{j}_\parallel - \frac{3}{2}\frac{T_e}{e\omega_e\tau_e B}\boldsymbol{B}\times\boldsymbol{j}_\perp \tag{C.10}$$

the energy exchange term between electrons and ions:

$$Q_{ei} = \frac{3m_e}{m_i}\frac{n_e}{\tau_e}\left(T_i - T_e\right) \tag{C.11}$$

and the transport coefficients.

To simulate SOL plasma in the magnetic field geometry of a tokamak, the Braginskii equations are written in a curvilinear orthogonal coordinate system. The x-coordinate varies along flux surfaces and the y-coordinate varies perpendicular to flux surfaces, z is the toroidal direction (see Fig. C.1). The equations transformed to the curvilinear orthogonal coordinates, the B2 equations, are described in [26].

Assuming toroidal symmetry greatly simplifies the problem and the B2.5 code solves the B2 equations in the poloidal plane. The simulation domain covering the SOL is discretized using quadrilateral cells (Fig. C.2).

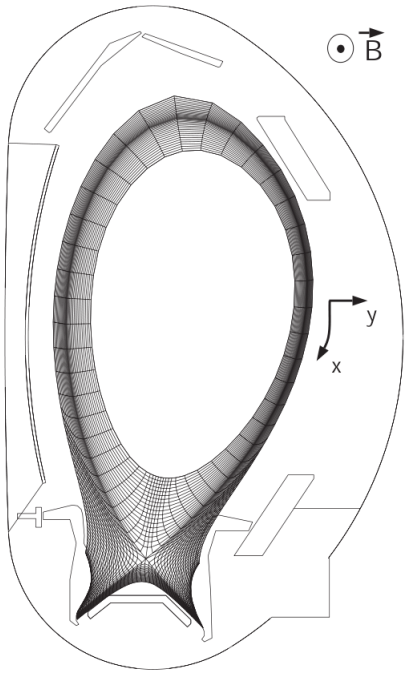

Figure C.1: The coordinate system used in B2.5 code.

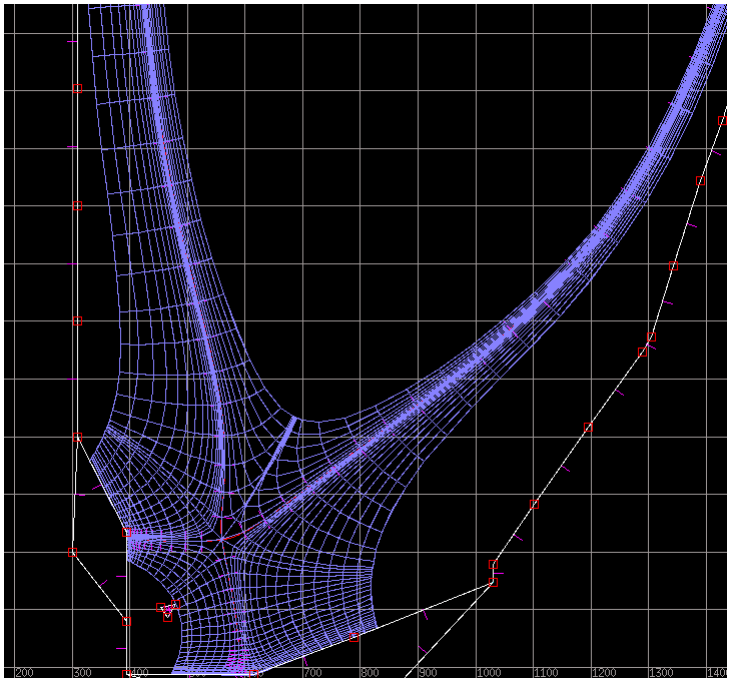

Figure C.2: An example of B2 mesh.

The boundary conditions are implemented in the B2.5 code by specifying conditions in the boundary cells (Fig. C.3). There are three types of boundaries: the target boundary, the core boundary and the outer boundary (outer SOL and outer private region). The specific types of boundary conditions used in the simulations for this research are outlined as follows.

- The ion momentum equation. At the core and the outer boundaries, the velocity is set to zero. At the target boundaries, the velocity is determined by the Bohm criterion which translates into

$$\boldsymbol{v}_{\parallel} = c_s \equiv \sqrt{\frac{k_B \left(Z_i T_e + T_i\right)}{m_i}} \tag{C.12}$$

  from which the $\boldsymbol{v}_x$ and the $\boldsymbol{v}_y$ components are then calculated based on the magnetic field angle.

- The continuity equation. At the core boundary, a zero flux condition is applied to simulate the particle balance between the core and the SOL in a steady state. At the outer boundaries, the decay length of the density is prescribed. At the target boundaries, the outgoing flux is determined by $\boldsymbol{\Gamma} = n\boldsymbol{v}_x$ based on the $\boldsymbol{v}_x$ obtained according to the Bohm criterion.

- The Ohm's law. At the core boundary, the current is set to zero. At the outer boundaries, the outgoing current is given by

$$j_y = \frac{1}{\sqrt{2\pi}} e n v_{th,e} \exp\left(-\frac{e\Phi}{k_B T_e}\right) \tag{C.13}$$

  where $v_{th,e} = \sqrt{k_B T_e / m_e}$ is the electron thermal velocity. At the target boundaries, the outgoing current is given by

$$j_x = en\left[b_x c_s - b_x \frac{1}{\sqrt{2\pi}} v_{th,e} \exp\left(-\frac{e\Phi}{k_B T_e}\right)(1-\gamma_e)\right] \tag{C.14}$$

  where γ_e is the secondary electron emission coefficient. The currents effectively determines charge sources at the boundary cells.

- The energy equations. At the core boundary, the total heat flux with constant flux density is prescribed. At the outer boundaries, the decay length of the

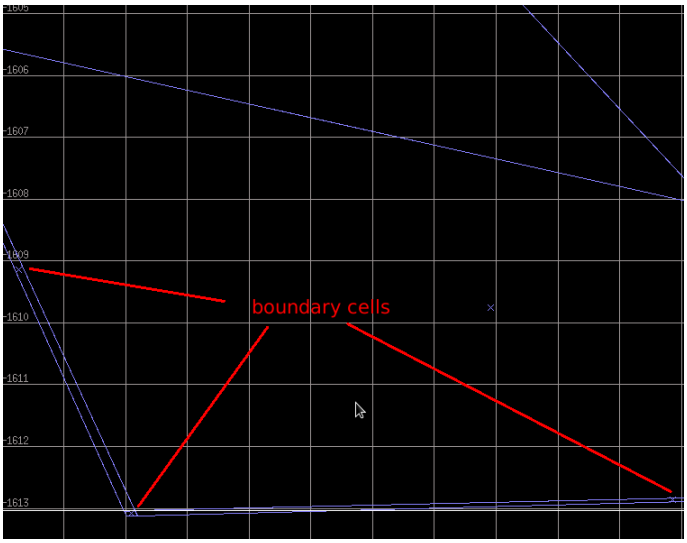

Figure C.3: Boundary cells of the B2 mesh.

temperature is prescribed. At the target boundaries, the outgoing heat flux is given by

$$q_{iz} = \frac{3}{2} n T_i c_s b_x \tag{C.15}$$

for ions and

$$q_{ex} = b_x \frac{n}{\sqrt{2\pi}} v_{th,e} \exp\left(-\frac{e\Phi}{k_B T_e}\right)(1-\gamma_e)\left(T_e \frac{1+\gamma_e}{1-\gamma_e} + e\Phi\right) \tag{C.16}$$

for electrons.

The conditions on the target boundaries are all determined by the sheath condition.

The various source terms in the B2 equations are computed based on the Eirene calculation for neutrals.

C.2 Eirene for Neutral Modeling

The transport of neutral atoms is modeled using the Eirene code [23] in SOLPS.

Neutral transport is described by the linearized Boltzmann equation,

$$\left[\frac{\partial}{\partial t} + \boldsymbol{v}\cdot\nabla + \frac{1}{m}\boldsymbol{F}\cdot\nabla_{\boldsymbol{v}}\right] f(\boldsymbol{r},\boldsymbol{v},t) + \Sigma(\boldsymbol{r},\boldsymbol{v})\,|\boldsymbol{v}|\, f(\boldsymbol{v}) = \int \mathrm{d}^3 v' C(\boldsymbol{r};\boldsymbol{v}'\to\boldsymbol{v})\,|\boldsymbol{v}'|\, f(\boldsymbol{v}') + Q(\boldsymbol{r},\boldsymbol{v},t) \tag{C.17}$$

where $\Sigma(\boldsymbol{r},\boldsymbol{v})$ is the macroscopic cross section and $Q(\boldsymbol{r},\boldsymbol{v},t)$ is any external source (particles injected per unit volume in phase space and per unit time). It is obtained by neglecting neutral-neutral collisions and keeping only neutral-plasma collision in the collision integral of the original Boltzmann equation. Thus the equation is linear in f since the distribution function for plasma is given (provided by B2.5 calculations). The loss due to neutral-plasma collision is separated from the integral and written as $\Sigma(\boldsymbol{r},\boldsymbol{v})|\boldsymbol{v}|f(\boldsymbol{v})$ with $\Sigma(\boldsymbol{r},\boldsymbol{v})$ independent of f.

Often the characteristic time constants for neutral particle transport phenomena are very short (μs), compared to those for plasma transport (ms). Therefore, explicit time dependence is often neglected in the equations describing the neutral particles. The transport equation (C.17) then reduces to the more compact form,

$$\nabla\Phi(\boldsymbol{r},\boldsymbol{v},t)+\Sigma(\boldsymbol{r},\boldsymbol{v})\Phi=\int \mathrm{d}^3v' C(\boldsymbol{r};\boldsymbol{v}'\rightarrow\boldsymbol{v})\Phi(\boldsymbol{v}')+Q(\boldsymbol{r},\boldsymbol{v},t) \tag{C.18}$$

where $\Phi(\boldsymbol{r},\boldsymbol{v},t)=|\boldsymbol{v}|f(\boldsymbol{r},\boldsymbol{v},t)$.

The Eirene code obtains statistical solutions to equation (C.18) using Monte Carlo method.

A discrete Markoff chain is defined using Q as an initial distribution and the collision kernel C as a transition probability. Histories ω^n from this stochastic process are generated according to $\omega^n=(x_0,x_1,...,x_n)$, (where $x_j=x_a$ for $j\geq n$ and $x_i\neq x_a$ for all $i\leq n$), with x_n being the first state after transition into the absorbing state x_a. x_0 denotes the initial state distributed as described by Q. The length n of the chain ω^n is itself a random variable. A random sampling procedure to generate such chains is carried out in Monte Carlo codes by converting machine generated (pseudo-) random numbers into random numbers with the distributions Q and C.

Usually, a detailed knowledge of Φ is not required, but only a set of "responses", R. Thus in the Eirene code, once N chains, ω_i, have been computed, the response R with respect to a detector function g is estimated as the arithmetic mean of functions ("estimators"),

$$R\equiv\int \mathrm{d}x\Phi(x)g(x)=\frac{1}{N}\sum_{i=1}^{N}X_g(\omega_i) \tag{C.19}$$

where there are a few choices of the unbiased estimators for X_g (see [23]). The arithmetic averaging is performed in each cell in the mesh specified by the user (Fig. C.4).

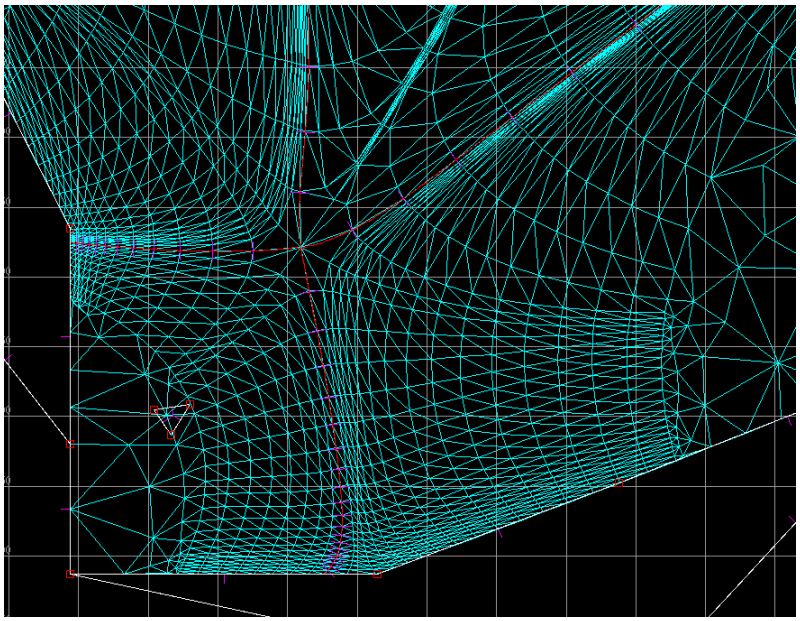

Figure C.4: An example of the triangular mesh for Eirene.

In a B2.5-Eirene coupled run, during each time step, the plasma quantities are calculated by B2.5 and provided to Eirene as a background from which the Σ and the C are determined. The plasma-neutral interactions contributes to part of the source $Q(\boldsymbol{r}, \boldsymbol{v}, t)$ with the remaining part being neutral gas puffing, pumping and recycling at the wall surface. With such information, Eirene computes the prescribed number of particle histories and estimates the responses. The plasma particle, momentum and energy sources from plasma-neutral interaction are then evaluated and passed to B2.5. The code then advances to the next iteration.

Bibliography

[1] D. Kacprzak, "Engineering Electromagnetics," University of Auckland, September 2001. [Online]. Available: http://homepages.engineering.auckland.ac.nz/kacprzak/notes.htm.

[2] H.-S. Bosch et. al., Extension of the AS-DEX Upgrade programme: Divertor-II and tungsten target plate experiment. Technical Report 1/281a, IPP, Garching, Germany, December 1994.

[3] R. Goldston, "Heuristic drift-based model for the power scrape-off width in H-mode tokamaks," in 38th EPS Conference on Plasma Physics, Strasbourg, France, 2011.

[4] "Fusion Energy: Magnetic Confinement," Department of Physics, University of York., 2013. [Online]. Available: http://www.york.ac.uk/physics/postgraduate/researchprojects/curren-research-projects/plasmaphysics/fusionplasmas/.

[5] Princeton Plasma Physics Laboratory, [Online]. Available: http://surface.pppl.gov/images/NSTX.png.

[6] "Ohmic Heating," EFDA, [Online]. Available: http://www.efda.org/fusion/focus- on/plasma-heating-current-drive/ohmic-heating/.

[7] S. Allen, V. Soukhanovskii, T. Osborne, E. Kolemen, J. Boedo, N. Brooks, M. Fenstermacher, R. Groebner, D. Hill, A. Hyatt, C. Lasnier, A. Leonard, M. Makowski, W. Meyer, A. McLean, T. Petrie, D. Ryutov, and J. Watkins. In *Proceedings of the 24th International Conference on Fusion Energy, San Diego, USA (International Atomic Energy Agency, Vienna, 2012)*, 2012.

[8] S.I. Braginskii. Transport processes in a plasma. Reviews of Plasma Physics, 1, 205–311, Consultants Bureau, New York, 1965.

[9] Brent Covele, Mike Kotschenreuther, Swadesh Mahajan, Prashant Valanju, A. Leonard, John Watkins, M. Makowski, and M. Fenstermacher. X-divertors for deeper detachment without degrading the diii-d h-mode. In *Proceedings of the 26th International Conference on Fusion Energy, Kyoto, Japan (International Atomic Energy Agency, Vienna, 2016)*, 2016.

[10] Brent Covele, Prashant Valanju, Mike Kotschenreuther, and Swadesh Mahajan. An exploration of advanced x-divertor scenarios on iter. *Nuclear Fusion*, 54(072006), 2014.

[11] Brent Michael Covele. *2-D Magnetic Equilibrium and Transport Modeling of the X-Divertor and Super X-Divertor for Scrape-Off Layer Heat Flux Mitigation in Tokamaks*. PhD thesis, University of Texas at Austin, 2014.

[12] J. Crotinger, L. LoDestro, L. Pearlstein, A. Tarditi, T. Casper, and E. Hooper. Llnl report ucrl-id-126284, 1997. available from NTIS PB2005-102154.

[13] S.P. Gerhardt, R. Andre, and J.E. Menard. Exploration of the equilibrium operating space for nstx-upgrade. *Nuclear Fusion*, 52(8):083020, 2012.

[14] H. Grad and H. Rubin. In Proc. of the Second United Nations Conference on the Peaceful Uses of Atomic Energy, volume 31, page 190, Geneva, 1958. Unite Nations.

[15] E. Havlíčková, M. Wischmeier, B. Lipschultz, and G. Fishpool. The effect of the super-x divertor of {MAST} upgrade on impurity radiation as modelled by {SOLPS}. *Journal of Nuclear Materials*, 463:1209 – 1213, 2015. PLASMA-SURFACE {INTERACTIONS} 21Proceedings of the 21st International Conference on Plasma-Surface Interactions in Controlled Fusion Devices Kanazawa, Japan May 26-30, 2014.

[16] M. Kotschenreuther, P. Valanju, S J. Wiley, T. Rognlein, Mahajan, and M. Pekker. In *Proceedings of the 20th International Conference on Fusion Energy, Vilamoura, Portugal (International Atomic Energy Agency, Vienna, 2004), IC/P6-43*, 2004.

[17] M. Kotschenreuther, P. Valanju, and S. Mahajan. *Bull. Am. Phys. Soc.*, 53:11, 2007.

[18] M. Kotschenreuther, P. Valanju, S. Mahajan, M. Pekker J. Wiley, W. Rowan, Huang He, T. Rognlein, and D. Gates. In *Proceedings of the 21st International Conference on Fusion Energy, Montpellier, France (International Atomic Energy Agency, Vienna, 2006), IC/P7-12*, 2006.

[19] M. Kotschenreuther, P. M. Valanju, S. M. Mahajan, and J. C. Wiley. On heat loading, novel divertors, and fusion reactors. *Physics of Plasmas*, 14(7):072502, 2007.

[20] Mike Kotschenreuther, Prashant Valanju, Brent Covele, and Swadesh Mahajan. Magnetic geometry and physics of advanced divertors: The x-divertor and the snowflake. *Physics of Plasmas*, 20(10):102507, 2013.

[21] J.E. Menard, S. Gerhardt, M. Bell, J. Bialek, A. Brooks, J. Canik, J. Chrzanowski, M. Denault, L. Dudek, D.A. Gates, N. Gorelenkov, W. Guttenfelder, R. Hatcher, J. Hosea, R. Kaita, S. Kaye, C. Kessel, E. Kolemen, H. Kugel, R. Maingi, M. Mardenfeld, D. Mueller, B. Nelson, C. Neumeyer, M. Ono, E. Perry, R. Ramakrishnan, R. Raman, Y. Ren, S. Sabbagh, M. Smith, V. Soukhanovskii, T. Stevenson, R. Strykowsky, D. Stutman, G. Taylor, P. Titus, K. Tresemer, K. Tritz, M. Viola, M. Williams, R. Woolley, H. Yuh, H. Zhang, Y. Zhai, A. Zolfaghari, and the NSTX Team. Overview of the physics and engineering design of nstx upgrade. *Nuclear Fusion*, 52(8):083015, 2012.

[22] F Piras, S Coda, I Furno, J-M Moret, R A Pitts, O Sauter, B Tal, G Turri, A Bencze, B P Duval, F Felici, A Pochelon, and C Zucca. Snowflake divertor plasmas on tcv. *Plasma Physics and Controlled Fusion*, 51(5):055009, 2009.

[23] D. Reiter. The eirene code user manua, 2009. Available online: http://www.eirene.de/.

[24] D. D. Ryutov. Geometrical properties of a "snowflake" divertor. *Physics of Plasmas*, 14(6):064502, 2007.

[25] D. D. Ryutov, R. H. Cohen, T. D. Rognlien, and M. V. Umansky. The magnetic field structure of a snowflake divertor. *Physics of Plasmas*, 15(9):092501, 2008.

[26] R. Schneider, X. Bonnin, K. Borrass, D. P. Coster, H. Kastelewicz, D. Reiter, V. A. Rozhansky, and B. J. Braams. Plasma edge physics with b2-eirene. *Contributions to Plasma Physics*, 46(1-2):3–191, 2006.

[27] V. A. Soukhanovskii, R. E. Bell, A. Diallo, S. Gerhardt, S. Kaye, E. Kolemen, B. P. LeBlanc, A. G. McLean, J. E. Menard, S. F. Paul, M. Podesta, R. Raman, T. D. Rognlien, A. L. Roquemore, D. D. Ryutov, F. Scotti, M. V. Umansky, D. Battaglia, M. G. Bell, D. A. Gates, R. Kaita, R. Maingi, D. Mueller, and S. A. Sabbagh. Snowflake divertor configuration studies in national spherical torus experiment. *Physics of Plasmas*, 19(8):082504, 2012.

[28] Peter C. Stangeby. *The Plasma Boundary of Magnetic Fusion Devices*. IOP Publishing Ltd., 2000.

[29] Haruhiko Takase. Guidance of divertor channel by cusp-like magnetic field for tokamak devices. *Journal of the Physical Society of Japan*, 70(3):609–612, 2001.

[30] P. Valanju, M. Kotschenreuther, and S. Mahajan. In *Invited talk at APS-DPP Meeting (2008)*, 2008.

[31] P. M. Valanju, M. Kotschenreuther, S. M. Mahajan, and J. Canik. Super-x divertors and high power density fusion devices. *Physics of Plasmas*, 16(5):056110, 2009.

[32] P.M. Valanju, M. Kotschenreuther, and S.M. Mahajan. Super x divertors for solving heat and neutron flux problems of fusion devices. *Fusion Engineering and Design*, 85(1):46 – 52, 2010.